Impact of Antenna Pattern on TOA Based 3D UAV Localization Using a Terrestrial Sensor Network

Priyanka Sinha and Ismail Guvenc
Department of Electrical and Computer Engineering, North Carolina State University, Raleigh, NC
Email: {psinha2,iguvenc}@ncsu.edu

***Abstract*—In this paper, we explore the fundamental limits of the 3-dimensional (3D) localization of unmanned aerial vehicles (UAVs) in conjunction with the effects of 3D antenna radiation patterns. Although localization of UAVs has been studied to some extent in the literature, effects of antenna characteristics on 3D localization remains mostly unexplored. To study such effects, we consider a scenario where a fixed number of radio-frequency (RF) sensors equipped with single or multiple dipole antennas are placed at some known locations on the ground, and they derive the time-difference-of-arrival (TDOA) measurements from the time-of-arrival (TOA) data collected for the UAV that is also equipped with a dipole antenna. We then use these measurements to estimate the 3D location of the UAV, and to derive the Cramer-Rao lower bounds (CRLBs) on the localization error for various orientations of the dipole antennas at the transmitter and the receiver. Namely, we consider vertical-vertical (VV), horizontal-horizontal (HH), and vertical-horizontal (VH) radiation patterns in a purely line-of-sight (LoS) environment and a mixed LoS/Non-line-of-sight (NLoS) environment. We show that the localization accuracy changes in a non-monotonic pattern with respect to the UAV altitude and identify the respective critical altitudes for each of the VV, VH and HH orientations. Subsequently, we propose a multi-antenna signal acquisition technique that mitigates the accuracy degradation due to the antenna pattern mismatches, and we derive the localization CRLB for the multi-antenna scenario. Our numerical results characterize achievable localization accuracy for various antenna configurations, UAV heights, and propagation conditions for representative UAV scenarios.**

***Index Terms*—Antenna pattern, Cramer-Rao lower bound (CRLB), drone localization, TDOA, unauthorized UAV.**

I. Introduction

Localization of unmanned aerial vehicles (UAVs) in a 3D airspace has a wide range of applications in military, commercial, government, and recreational scenarios. Depending on the context, the UAV may or may not participate in the localization process, either because the UAV communication system might not be designed for positioning purposes, or it may be a non-cooperating and potentially a malicious UAV [1]–[3]. Whether the goal is to localize a cooperating or a non-cooperating UAV, there are several parameters associated with an RF signal [2]–[5] that can be captured from a UAV at multiple sensor locations, such as the received signal strength (RSS), angle-of-arrival (AOA), time-of-arrival (TOA), and time difference of arrival (TDOA) [6]. Those measurements can then be fused by a centralized unit for localizing and tracking the target UAV.

This work has been supported in part by NASA and NSF under the Federal Award numbers NX17AJ94A and CNS-1814727, respectively.

Due to the simplicity of implementation, localization schemes involving RSS, TOA, and TDOA are more common as compared to the AOA methods, and the time based methods are usually preferred over the RSS based methods due to the higher degree of accuracy they provide. Between the TOA and the TDOA based approaches, TDOA is more suitable to a wider range of general applications including localization of unauthorized UAVs, as it does not require the source clock to be synchronized with that of the RF sensor. We therefore focus on TDOA based localization in this rest of this paper.

There are various technical challenges for accurate 3D localization of UAVs that rely on TDOA measurements. Since air-to-ground (A2G) links have higher likelihood of being a line-of-sight (LoS) link, the link quality is also highly sensitive to any possible mismatches in the antenna patterns at the transmitter and the receiver. As a result, the signal to noise ratio (SNR) of an A2G link can degrade rapidly with slight changes in the transmit and the receive antenna orientations and the mobility of the UAV [7]. Since the quality of the TDOA measurements are dependent on the SNR of the target A2G link, it is important to take the 3D antenna patterns into account while designing a robust 3D localization algorithm. Moreover, the performance of the time-based localization methods are known to suffer in a non-LoS (NLoS) environment [8], [9], due to the introduction of a positive bias in the localization error. Thus the localization accuracy of the UAVs may significantly degrade in a densely built up urban environment due to the diminished likelihood of the LoS propagation.

In this paper, which is a rigorously extended version of our earlier work in [10], we develop a unified analytical framework which jointly takes into account the impact of the 3D antenna patterns and the probabilistic LoS/NLoS nature of the A2G links on the accuracy of TDOA-based 3D UAV localization. To our best knowledge, such a unified framework and analysis is not available in the existing literature. While in [10] we only consider a single antenna signal acquisition technique in the presence of a purely LoS A2G channel, in this work we study both the single and the multi-antenna techniques in a purely LoS environment and a mixed LoS/NLoS environment. Our key contributions can be listed as follows.

- Considering single transmit and receive antennas at the UAV and the ground sensors, we derive the Cramer-Rao lower bounds (CRLBs) for TDOA-based 3D localization of UAVs for three different antenna orientations, namely, VV, VH, and HH.

- In addition to considering purely LoS A2G links, we also derive the CRLBs on 3D UAV localization accuracy for mixed LoS/NLoS A2G links.
- As a mitigation technique, we consider localization by ground sensors with multiple receive antennas, and we derive the CRLB for the multi-antenna radiation patterns.
- Our numerical results characterize the achievable 3D localization accuracy of UAVs for various scenarios and reveal several insights, such as the non-monotonic behavior of localization accuracy with respect to the UAV altitude and the critical altitudes that optimize the localization accuracy for a given scenario.

The rest of this paper is organized as follows. In Section II, we provide an overview of the related literature on 3D localization to place our contributions in context. In Section III, we describe the system model capturing the network topology, A2G propagation, and 3D radiation patterns. In Section IV, we derive the statistical properties of the TOA measurements, and establish the dependence of the TOA variance on the antenna patterns. Using these findings, Section V derives the distribution of the TDOA measurements extracted from the TOA measurements, and subsequently, the 3D localization CRLB is derived in Section VI. In Section VII, we present numerical results that consider both theoretical bounds as well as a gradient-descent based location estimator for various scenarios. Finally the paper is concluded in Section VIII.

II. Literature Review

State of the art RF localization methods typically use approaches such as radio frequency identification, ultra wideband positioning (UWB), cellular network based positioning, or wireless local area network based positioning, which are all applicable to localizing UAVs. There are scenarios where UAVs are localized through dedicated signaling (see e.g. [32]), while in some other scenarios sensors are required to passively intercept the wireless signal exchange between the UAV and its ground controller (GC) [15], [33], [34]. In either scenario, sensors with an omni-directional radiation on the horizontal plane can provide good localization coverage as long as UAVs fly at a close enough altitude with the sensor antennas. However, for scenarios where UAVs may fly at a wide range of different altitudes from the ground, it is difficult to maintain omni-directional radiation across the whole volume where UAVs are expected to fly. For example, despite the high density of sub 6 GHz cellular base stations (BSs), the downtilted antenna pattern at these BSs that are optimized to serve terrestrial users will result in very poor localization performance when trying to localize UAVs at higher altitudes.

In order to maintain communication with the GCs throughout the UAV flight, typically, dipole antennas are used at the UAV and the GC, which have an omni-directional radiation pattern in the horizontal plane. There are many papers in the literature that experimentally study the degradation in communication performance due to the use of dipole antennas for different UAV altitudes, see e.g. [7], [11]–[14]. However, to our best knowledge, such antenna effects have not been studied in the existing literature from a 3D UAV localization perspective other than our earlier preliminary work in [10]. There is hence a gap in the literature on the characterization of 3D UAV localization accuracy considering different antenna patterns and orientations.

In most of the existing related literature, the problem of 3D localization is studied in the context of a generic wireless sensor network (WSN). Papers such as [16], [18]–[21] construct novel 3D location estimators from RSS and/or AOA measurements for generic 3D targets, under propagation conditions that assume constant presence of a LoS component in conjunction with log normal shadowing. While such works are not directly applicable to localization of UAVs, due to the lack of an appropriate A2G channel model (which is probabilistic and mixed LoS/NLoS in nature), they also fail to account for any realistic antenna patterns. Moreover the authors only compare the performance of their proposed estimators against state-of-the art techniques, and do not provide any theoretical characterization and fundamental bounds.

In [17], [22], although the authors derive both the CRLB and an estimator for an emitter's location, they still consider less than realistic LoS channel model and isotropic antenna patterns. In a similar line of work, [23], [30], [31] derive location estimators using sensor networks of different kinds, such as a UWB sensor network and a vehicular ad-hoc network (VANET), respectively. Although all of these works consider a more realistic 3D channel, composed of both LoS and NLoS components, they do not consider any realistic antenna patterns. Finally, in [29] the authors derive the CRLB on 3D localization for a visible light communication (VLC) sensor network and theoretically characterize the impact of Lambertian [35] (directional) radiation pattern on the accuracy. However, this work is not applicable to localization of UAVs that use RF links for communication, due to the significant difference between the characteristics of the wireless RF channels and wireless optical channels [35].

In [24]–[28], authors consider cellular BSs as the sensor network for 3D localization. Although most BSs have a vertically downtitlted antenna pattern, the authors in [24], [26], [27] do not consider any realistic antenna pattern. While [24] derives the CRLB for the RSS-based localization for a UAV in particular, it fails to account for a realistic antenna pattern, and only considers purely LoS A2G links, which can deviate significantly from the true nature of the A2G links in urban environments. In [25], the authors use TDOA measurements from a network of cellular BSs to localize UAVs in the presence of a mixed LoS/NLoS channel, and characterize the probability of localization. However they do not consider the the realistic downtilted antenna patterns that most terrestrial cellular BSs are equipped with, and they do not provide a theoretical characterization of the localization error. Lastly, in [28] the authors consider the antenna patterns for uniform planar array (UPA) at the BS, in conjunction with a mixed LoS/NLoS channel, but only location estimators were derived, and the impact of the antenna pattern on the localization performance was not considered.

For easier comparison of the contributions of our work on 3D localization, we provide an overview of the related

TABLE I: Related work on 3D localization and the impact of 3D antenna patterns (AOD: angle of departure, IMU: intertial measurement unit, ADCPM: angle-delay domain channel power matrix, AP: access point).

Paper	Infrastructure	Measurement	Channel Model	Antenna Pattern	Localized Node	Contribution
[7], [11]–[14]	WiFi	RSS	LoS	Dipole, WiMo 18720.11	N/A, focus is on UAV 3D link reliability	Experimental analysis of 3D dipole antenna patterns
[15]	Passive RF sensor network	TDOA	LoS	Omni-directional broadband	UAV in 3D space	Experimental analysis of 3D localization accuracy
[16]	WSN	RSS, AOA	LoS/Shadowing	Isotropic	Generic 3D target	Location estimator
[17]	WSN	RSS, AOA	LoS/Shadowing	Isotropic	UAV in 3D space	Location estimator, CRLB
[18]	WSN	RSS	LoS	Isotropic	Generic 3D target	Location estimator
[19], [20]	WSN	RSS, AOA	LoS/Shadowing	Isotropic	Generic 3D target	Location estimator
[21]	WSN	RSS	LoS/Shadowing	Isotropic	Generic 3D target	Location estimator
[22]	WSN	RSS/TOA, AOA	LoS	Isotropic	Generic 3D target	Location estimator, CRLB
[23]	WSN (UWB)	TOA, TDOA	IEEE 802.15.4a LoS/NLoS	Isotropic	Generic 3D target	Location estimator
[24]	Cellular network	RSS	Deterministic LoS	Isotropic	UAV in 3D space	CRLB
[25]	Cellular network	TDOA	LoS/NLoS	Isotropic	UAV in 3D space	Localizability
[26]	Single BS	AOD, AOA, TOA	Indoor NLoS	Isotropic	3D mobile station	Location estimator, CRLB
[27]	Single BS	TOA/IMU	LoS	Isotropic	3D mobile station	CRLB
[28]	Single BS	ADCPM	LoS/NLoS	UPA	Generic 3D target	Location estimator
[29]	VLC Access Points	RSS, AOA	Wireless optical channels	Lambertian	VLC receiver in 3D space	CRLB with directional beam patterns
[30], [31]	VANET	TOA, RSS, AOA	LoS/NLoS	Isotropic	3D vehicular node	Location estimator
Our work	WSN	TDOA	LoS/NLoS	Dipole	UAV in 3D space	CRLB with 3D antenna patterns and LoS/NLoS

literature on 3D localization in
of the key characteristics of ou

III. Syst

We consider a sensor netwo
(FTs), where the i^{th} sensor i
$(x_i, y_i, 0)$, with $1 \leq i \leq N$. Eac
TOA measurements from the
located at an unknown locatio
sensors might be equipped witl
tally oriented dipole antenna or
dipole antennas. The UAV is a
horizontally oriented dipole an
model with three ($N = 3$) grou
the unknown 3-D location coo
and evaluate the impact of tl
on the said localization perfo
we denote the 3D and the tw
between the UAV and the i^{th} sensor, as α_i and r_i.

$$d_i = \sqrt{(x_i - x)^2 + (y_i - y)^2 + h^2} \ ,$$
$$r_i = \sqrt{(x_i - x)^2 + (y_i - y)^2} \ . \quad (1)$$

The elevation and the azimuth angles associated with i^{th} sensor are denoted respectively as α_i and ϕ_i, given by:

$$\alpha_i = \tan^{-1}\left(\frac{h}{r_i}\right) \ , \ \phi_i = \tan^{-1}\left(\frac{y - y_i}{x - x_i}\right) \ . \quad (2)$$

A. Propagation Channel Model

The A2G links usually tend to have a line-of-sight (LoS) component, giving rise to a mixed LoS/NLoS channel. Due to the lower availability of scattering and blocking objects in the case of a 3D channel, the probability of having a LoS path in an A2G channel is usually larger than that of terrestrial channels. Thus in this paper we model all the A2G

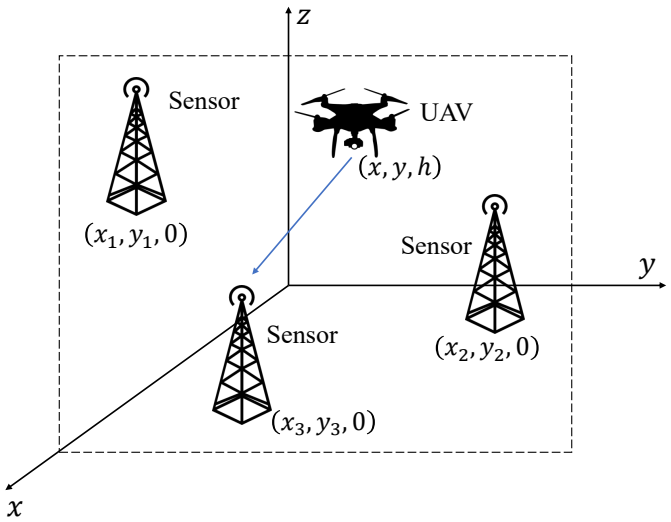

Fig. 1: Reference sensors with fixed locations, that collect TOA measurements for UAV localization.

links between the ground sensors and the target UAV, to be of mixed LoS/NLoS nature. For the characterization of the mixed LoS/NLoS A2G links, we adopt the model in [36], that represents the total path loss in an A2G link, as the sum of the free space path loss, and an additional path loss ($\eta^{\mathsf{S_A}}$) due to the reflections, scattering and shadowing in the environment, depending on the state, $\mathsf{S_A} \in \{\mathsf{LoS}, \mathsf{NLoS}\}$ of the given A2G link, where $\eta^{\mathsf{NLoS}} > \eta^{\mathsf{LoS}}$ [36]. Thus, the path loss over the i^{th} A2G link is given in the dB scale as [36]:

$$\mathsf{PL}^{\mathsf{s_A}} = 20\log(d_i) + 20\log\left(\frac{4\pi f_{\mathsf{c}}}{\mathsf{c}}\right) + 20\log(\eta^{\mathsf{s_A}}) \ , \quad (3)$$

where f_{c} is the frequency of transmission from the unauthorized UAV and c is the speed of light. The probability that the A2G link between the UAV and the i^{th} ground sensor

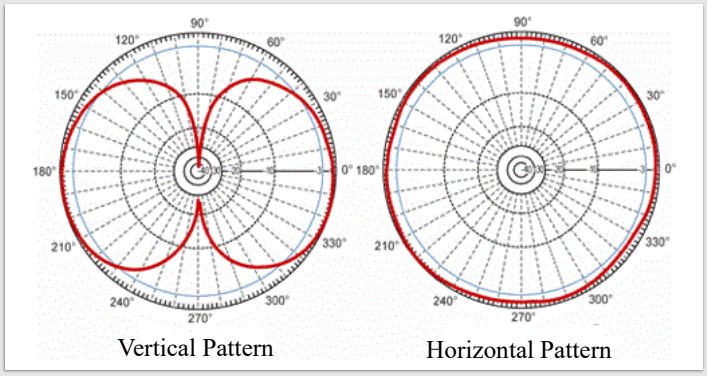

Fig. 2: Radiation pattern of a vertically oriented dipole antenna on the horizontal and the vertical planes.

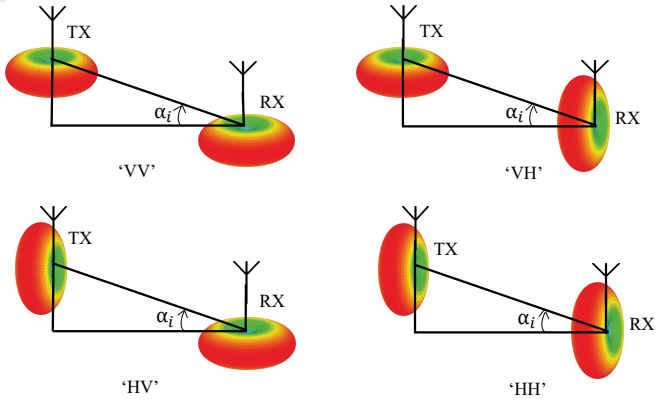

Fig. 3: Different radiation patterns arising from different antenna orientations at the transmitter (UAV) and the receiver (ground sensor). The combined antenna gain is the product of transmit and receive antenna gains across the A2G link.

will have a LoS path is described [36] as a function of the respective elevation angle, α_i, shown in (2):

$$\mathsf{P}_{\mathsf{LoS}}(\alpha_i) = \frac{1}{1 + b\exp\left\{-c[\frac{180}{\pi}(\alpha_i) - b]\right\}}, \quad (4)$$

where b and c are constants which depend on the environment, r_i is the horizontal distance between the UAV and the ground sensor, and h is the altitude of the UAV. The probability of the A2G link being in the NLoS state is given as: $1 - \mathsf{P}_{\mathsf{LoS}}(\alpha_i)$. We note that, in this model, the probability of having a LoS path for an A2G channel increases with the increasing altitude of the aerial object. For this work, we consider two different A2G environments, namely, a suburban (SU), and an urban (U), mentioned in the order of decreasing LoS dominance.

B. Realistic 3D Dipole Antenna Pattern

In order to study the impact of the dipole antenna radiation patterns on the TOA CRLB, we characterize the relationship between the total antenna gain experienced at the i^{th} sensor, and the variance of the TOA measurement noise at the i^{th} sensor. Fig. 2(a) and Fig. 2(b) demonstrate the radiation pattern of a vertically oriented (i.e. placed along the z-axis) dipole antenna located at $(x_i, y_i, 0)$, in the azimuth and the elevation plane, respectively. We note that the radiation pattern for the vertical orientation, denoted as, $G_z(\phi_i, \alpha_i)$, is omni-directional in the azimuth plane and doughnut-shaped in the elevation plane. Conversely, when the dipole antenna is horizontally oriented (i.e. placed along the y-axis), the resultant radiation pattern, denoted as $G_y(\phi_i, \alpha_i)$, has an omni-directional component in the vertical plane and a doughnut-shaped component in the horizontal plane. More specifically, $G_z(\phi_i, \alpha_i)$ and $G_y(\phi_i, \alpha_i)$ are described as [37]:

$$G_z(\phi_i, \alpha_i) = \frac{\cos\left(\frac{\pi l f_c}{c}\sin(\alpha_i)\right) - \cos(\frac{\pi f_c l}{c})}{\cos(\alpha_i)}, \quad (5)$$

$$G_y(\phi_i, \alpha_i) = \frac{\cos(\frac{\pi l f_c}{c}\cos(\cos^{-1}(\cos(\alpha_i)\sin(\phi_i))))}{\sin(\cos^{-1}(\sin(\phi_i)\cos(\alpha_i)))} - \frac{\cos(\frac{\pi f_c l}{c})}{\sin(\cos^{-1}(\sin(\phi_i)\cos(\alpha_i)))}, \quad (6)$$

where l is the length of the dipole antenna and f_c is the frequency of transmission. In the rest of the paper we specifically consider a half-wave dipole antenna, and thus $l = \frac{\lambda}{2}$, where $\lambda = \frac{c}{f_c}$ is the wavelength. We refer to this description of the 3D radiation patterns of a dipole antenna, given by (5) and (6), as the Model-1.

For a 3D single input single output (SISO) link, where the transmitter and the receiver are each equipped with a single antenna, we consider the 4 possible antenna orientations. In particular, we have the VV pattern, where both the transmit and the receive antennas are oriented vertically, the HH pattern, where both the transmit and the receive antennas are oriented horizontally, and the VH pattern, where the transmit and the receive antennas are respectively, vertically and horizontally oriented (see e.g. [7], [11], [12] for similar analysis). The transmit gain, $G_{\text{TX}}(\phi_i, \alpha_i)$ and the receive gain, $G_{\text{RX}}(\phi_i, \alpha_i)$ for the different orientations are summarized in the left half of Table II, where the total antenna gain experienced by the i^{th} A2G link can be obtained by the product of the transmit and the receive gain $G_{\text{TX}}(\phi_i, \alpha_i)G_{\text{RX}}(\phi_i, \alpha_i)$. The reason that we do not explicitly consider the HV antenna orientation case is because the total antenna gain (i.e. the the product of the transmit and the receive gain $G_{\text{TX}}(\phi_i, \alpha_i)G_{\text{RX}}(\phi_i, \alpha_i)$) in this case is the same as in the case of the VH orientation, and will yield same outcomes.

TABLE II: Transmit and receive antenna gains for the different antenna orientations in Fig. 3 with the realistic and approximated antenna patterns.

Model-1	**VV**	**VH**	**HH**
$G_{\text{TX}}(\phi_i, \alpha_i)$	$G_{\text{z}}(\phi_i, \alpha_i)$	$G_{\text{z}}(\phi_i, \alpha_i)$	$G_{\text{y}}(\phi_i, \alpha_i)$
$G_{\text{RX}}(\phi_i, \alpha_i)$	$G_{\text{z}}(\phi_i, \alpha_i)$	$G_{\text{y}}(\phi_i, \alpha_i)$	$G_{\text{y}}(\phi_i, \alpha_i)$
Model-2	**VV**	**VH**	**HH**
$G_{\text{TX}}(\phi_i, \alpha_i)$	$\cos(\alpha_i)$	$\cos(\alpha_i)$	$\sin(\alpha_i)$
$G_{\text{RX}}(\phi_i, \alpha_i)$	$\cos(\alpha_i)$	$\sin(\alpha_i)$	$\sin(\alpha_i)$

C. Approximated 3D Dipole Antenna Pattern Model

In addition to the realistic dipole antenna pattern, we also introduce a simpler approximation of the dipole antenna gain for the VV, HH and VH orientations described in the last section, and analyze the performance gap. In particular we

adopt the the approximation of the dipole antenna gains described in [38], [39]. Here the dipole antenna gain is approximated as a sine/cosine function of the elevation angle (α_i) between the aerial transmitter (the UAV), and the receiver at the i^{th} ground sensor depending on the orientation of the transmit and receive antennas. We refer to this description of the 3D radiation patterns of a dipole antenna, as the Model-2. Fig. 3(a) and Fig. 3(b), respectively show the antenna radiation patterns for the VV and the HH scenario. The VH and the HV patterns are identical in terms of the total antenna gain, and are illustrated in Fig. 3(c) and Fig. 3(d), respectively. The total antenna gain experienced by the the i^{th} A2G link can be obtained by the product of the transmit and the receive gain $G_{\text{TX}}(\phi_i, \alpha_i)G_{\text{RX}}(\phi_i, \alpha_i)$, and individual gains can be extracted from Table II for a given orientation.

IV. Impact of Antenna Orientations on TOA Distribution

In the first step of the localization process, we extract the time-of-arrival (TOA) measurements from the UAV signal received by each of the ground sensors in the network. Then the position of the target UAV is estimated based on the TDOA observations, which in turn are obtained by calculating the difference between the TOA estimates measured by a pair of time synchronized sensors. In this section we substantiate a relation between the variance of the TOA estimates and the total antenna gains, and thereby establish the dependency of the TDOA-based localization performance on the various antenna orientations.

A. TOA Measurements in Purely LoS Environment

We assume that each of the ground sensors in the network intercepts the UAV signal within the time interval $(0, T)$, where the UAV signal assumed to be transmitted for a duration of $T_s \leq T$, starting from an unknown time $t_0 \leq T$. In presence of a purely LoS A2G link, the signal received at the i^{th} sensor is given as:

$$r_i(t) = A_i s(t - \tau_i) + n(t) \ , \tag{7}$$

where τ_i is the true value of the TOA at the i^{th} sensor, $s(t)$ is the unit-energy pulse shaping signal, A_i is the amplitude factor representing large scale fading, and $n(t)$ is the additive white Gaussian noise (AWGN) at the receiver with zero mean and spectral density $\frac{N_0}{2}$. Let $\hat{\tau}_i$ be the measured value of the TOA of the UAV signal at the i^{th} ground sensor, given as:

$$\hat{\tau_i} = \tau_i + n_i \ , \quad \text{and} \quad \tau_i = \frac{d_i}{\text{c}} + t_0 \ , \tag{8}$$

where $n_i \sim \mathcal{N}(0, \sigma_i^2)$ is the additive measurement noise, and c is the speed of propagation.

In the literature, the maximum likelihood estimates (MLEs) of the TOAs in a LoS environment, are established as unbiased estimates with a zero-mean Gaussian noise, that achieves the CRLB. Thus the lower bound on the variance σ_i^2 of the TOA estimate $\hat{\tau}_i$ is given as [6], [40]:

$${\sigma_i}^2 \geq \frac{1}{2\sqrt{2}\pi\beta\Gamma_i} = \frac{k}{\Gamma_i} \ , \tag{9}$$

where β is the effective UAV signal bandwidth, and $\Gamma_i = \frac{{A_i}^2 E_{\text{s}}}{N_0}$ is the SNR of received signal at the i^{th} sensor, with E_s representing the energy in the transmit pulse shaping signal $s(t)$ (i.e. $E_{\text{s}} = 1$). For the broader objective of this paper, we summarize the impact of factors other than the SNR on the TOA measurement noise, using a proportionality constant k. Using the antenna gains described in Table II and following the free scale path loss model, the SNR of the i^{th} A2G link, in a purely LoS environment, is given in terms of the total received power, $P_{\text{RX}}(\alpha_i, \phi_i)$ (i.e. ${A_i}^2$):

$$\Gamma_i = \frac{P_{\text{RX}}(\alpha_i, , \phi_i)}{{\sigma_{\text{n}}}^2} = \left(\frac{\lambda}{4\pi}\right)^2 \frac{P_{\text{TX}} G_{\text{TX}}(\alpha_i, \phi_i) G_{\text{RX}}(\alpha_i, \phi_i)}{{\sigma_{\text{n}}}^2 {d_i}^2} \ , \tag{10}$$

where ${\sigma_{\text{n}}}^2$ is the variance of the thermal AWGN, P_{TX} is the transmitted signal power at the UAV.

Next, using (9), the relationship between the total antenna gain, and the variance of the TOA measurement noise at the i^{th} sensor is given as:

$${\sigma_i}^2 = \frac{k_0 {d_i}^2}{G_{\text{TX}}(\alpha_i, \phi_i) G_{\text{RX}}(\alpha_i, \phi_i)} \ , \tag{11}$$

where the proportionality constant k_0 summarizes the impact of all the factors other than the total antenna gain, and the 3D link distance, and is given as $k_0 = \frac{2{\sigma_{\text{n}}}^2 {f_{\text{c}}}^2}{P_{\text{TX}} \beta^2 c^2}$ [41].

1) TOA Measurements with Single Antenna Techniques: Given the relationship between the total antenna gains of the A2G link and the variance of the respective TOA measurement in (11), we now state the TOA variance for the case where the UAV and each of the ground sensors is equipped with a single dipole antenna. The variances of the TOA measurement between the UAV location (x, y, h) and the i^{th} sensor location $(x_i, y_i, 0)$, in a purely LoS environment, for the VV, HH and the VH orientations with Model-1 are given as:

$$\sigma^2_{\text{i-VV}} = \frac{k_0 {d_i}^2 \cos^2(\alpha_i)}{\cos^2(\pi k_{\text{l}} \sin(\alpha_i))} \ , \tag{12}$$

$$\sigma^2_{\text{i-HH}} = \frac{k_0 {d_i}^2 \sin^2(\cos^{-1}(\cos(\alpha_i)\sin(\phi_i)))}{\cos^2(\pi k_{\text{l}} \cos(\alpha_i)\sin(\phi_i))} \ , \tag{13}$$

$$\sigma^2_{\text{i-VH}} = \frac{k_0 {d_i}^2 \cos(\alpha_i)\sin(\cos^{-1}(\cos(\alpha_i)\sin(\phi_i)))}{\cos(\pi k_{\text{l}} \sin(\alpha_i))\cos(\pi k_{\text{l}} \cos(\alpha_i)\sin(\phi_i))} \ . \tag{14}$$

These are obtained after replacing $l = \frac{\lambda}{2}$ into (5) and (6), and computing the total antenna gains, $G_{\text{TX}}(\phi_i, \alpha_i)G_{\text{RX}}(\phi_i, \alpha_i)$, according to Model-1 in Table II. Substituting $G_{\text{TX}}(\phi_i, \alpha_i)G_{\text{RX}}(\phi_i, \alpha_i)$ into (11) yields (12)-(14).

Following similar steps for Model-2 described in the second half of Table II, the TOA variances with Model-2 for antenna radiation can be calculated as:

$$\sigma^2_{\text{i-VV}} = \frac{k_0 {d_i}^2}{\cos^2(\alpha_i)} \ , \ \sigma^2_{\text{i-HH}} = \frac{k_0 {d_i}^2}{\sin^2(\alpha_i)} \ , \ \sigma^2_{\text{i-VH}} = \frac{k_0 {d_i}^2}{\sin(\alpha_i)\cos(\alpha_i)} \ . \tag{15}$$

2) TOA Measurements with Multiple Antenna Techniques: In order to mitigate the orientation mismatches between the transmit and the receive antennas, we employ a multi-antenna technique at the ground receivers. This allows us to leverage the pattern and the orientation diversity by receiving two different versions of the transmitted signal via two receive antennas with two different orientations. Thus we now consider a 3D multiple input single output (MISO) link, where the transmitter is equipped with only one antenna but the receiver is equipped with two orthogonal dipole antennas, (one oriented vertically and another oriented horizontally), and characterize the receive gain at the i^{th} ground receiver, ($G_{\mathsf{H-V}}$), as $G_{\mathsf{V}}(\alpha_i, \phi_i) + jG_{\mathsf{H}}(\alpha_i, \phi_i)$ [42]. Here, each of the single dipole antenna patterns can be modeled according to the antenna patterns described in Table II. Finally for the two possible orientations of the single dipole antenna at the UAV (either vertical (V) or horizontal (H)), there are two possible total antenna gain patterns, denoted respectively, as $G_{\mathsf{V-HV}}$ and $G_{\mathsf{H-HV}}$.

Lemma 1: The variances of the i^{th} TOA measurements, in the cases, where the ground sensor is equipped with two orthogonally oriented antennas, and the UAV antenna is either vertically or horizontally orientated, are denoted respectively as $\sigma^2_{\text{i-V-HV}}$ and $\sigma^2_{\text{i-H-HV}}$, and are expressed as:

$$\sigma^2_{\text{i-H-HV}} = \frac{\sigma^2_{\text{i-HH}}\sigma_{\text{i-VV}}}{(\sigma^2_{\text{i-HH}} + \sigma^2_{\text{i-VV}})^{\frac{1}{2}}} \ , \ \sigma^2_{\text{i-V-HV}} = \frac{\sigma^2_{\text{i-VV}}\sigma_{\text{i-HH}}}{(\sigma^2_{\text{i-HH}} + \sigma^2_{\text{i-VV}})^{\frac{1}{2}}} \ . \quad (16)$$

Note that $\sigma^2_{\text{i-HH}}$ and $\sigma^2_{\text{i-VV}}$ can be obtained in closed form by using (14) for the realistic dipole antenna pattern and (15) for the approximated antenna pattern.

Proof: See Appendix A. ∎

B. TOA Measurements in a Mixed LoS/NLoS Environment

Although the TOA measurement noise in a purely LoS environment can be modelled as a zero-mean Gaussian random variable whose variance is given by (9), the TOA extraction in the NLoS situation, results in biased TOA estimates [43]. This is due to the fact that the multipath components in a NLoS environment, travel more than the LoS distance to reach the intended receivers. In addition, the TOA estimates in a mixed propagation environment have higher variance, compared to the TOA variance in a purely LoS environment, as the total path loss experienced by the UAV signal in a mixed propagation environment (as indicated by (3)) is slightly higher. Thus in a mixed propagation environment where the NLoS bias has the Gaussian distribution $\mathcal{N}(\mu_{\mathsf{b}}, \sigma^2_{\mathsf{b}})$, the distribution of the TOA measurement for a given location of the UAV $\boldsymbol{x} = (x, y, h)$, as collected by the i^{th} sensor located at $\boldsymbol{x_i} = (x_i, y_i, 0)$ is given as:

$$\hat{\tau}_i \sim \begin{cases} \mathcal{N}(\tau_i, \eta^{\mathsf{LoS}}\sigma_i^2) \ , & \text{with } \mathsf{P}_{\mathsf{LoS}}(\boldsymbol{x}, \boldsymbol{x_i}) \\ \mathcal{N}(\tau_i + \mu_{\mathsf{b}}, \eta^{\mathsf{NLoS}}\sigma_i^2 + \sigma^2_{\mathsf{b}}) \ , & \text{with } 1 - \mathsf{P}_{\mathsf{LoS}}(\boldsymbol{x}, \boldsymbol{x_i}) \end{cases} , \quad (17)$$

where η^{NLoS}, τ_i and ${\sigma_i}^2$ are obtained, respectively, from (3), (8) and (11).

V. Distribution of The TDOA Measurements

Having derived the distribution of the TOA measurements in the last section, we now obtain the distribution of the associated TDOA measurements.

A. Conditional Distribution of the TDOA Measurements in a Mixed LoS/NLoS Environment

Since TDOA measurements are obtained by computing the difference between the respective TOA measurements, using (8), the true and the estimated values of a TDOA observation, τ_{ij} and $\hat{\tau}_{ij}$, as collected by the i^{th} and the j^{th} sensors can be given as:

$$\tau_{ij} = \frac{d_i}{c} - \frac{d_j}{c} \ , \quad \hat{\tau}_{ij} = \hat{\tau}_i - \hat{\tau}_j \ . \quad (18)$$

From (17) and (18) we note that the distribution of the TDOA measurements depend on the particular propagation states (i.e. $\mathsf{S}_{\mathsf{A},i}$ and $\mathsf{S}_{\mathsf{A},j}$) of the two associated A2G links, and describe the TDOA distribution in the following lemma.

Lemma 2: Under a mixed LoS/NLoS environment, where the NLoS biases, $\{b_i\}$ at all sensors are independent and identically distributed (i.i.d) according to the Gaussian distribution: $b_i \sim \mathcal{N}(\mu_{\mathsf{b}}, \sigma^2_{\mathsf{b}})$, for $1 \leq i \leq N$, the *conditional distribution* of a *single TDOA measurement* for a given UAV location $\boldsymbol{x} = (x, y, h)$, collected by the i^{th} and the j^{th} sensors, while in the propagation states $\mathsf{S}_{\mathsf{A},i}$ and $\mathsf{S}_{\mathsf{A},j}$, respectively, is given in (19).

Proof: See Appendix B. ∎

In this paper, we choose the 1^{st} sensor, as shown in Fig. 1, as the reference sensor, and subtract the TOA measurement, $\hat{\tau}_1$, from all other TOA measurements, $\{\hat{\tau}_i\}$ for $2 \leq i \leq N$. Thus, we obtain the TDOA measurement vector $\boldsymbol{z} = [\hat{\tau}_{12}, \hat{\tau}_{13} ... \hat{\tau}_{1N}] \in \mathbb{R}^{(N-1)\times 1}$. Due to having a common reference sensor, the TDOA measurements are not independent, and the dependence is modeled through the covariance matrix $\boldsymbol{R}(\mathbf{x}) \in \mathbb{R}^{(N-1)\times(N-1)}$. We also note that the distribution of $\boldsymbol{z}$ is also dependent on the propagation states of all the sensors $\{\mathsf{S}_{\mathsf{A},i}\}$ for $1 \leq i \leq N$. For the ease of explanation we define a N-element random vector $\boldsymbol{S} : \Omega \rightarrow \{\mathsf{LoS}, \mathsf{NLoS}\}^N$, where $\boldsymbol{S}(i) = \mathsf{S}_{\mathsf{A},i}$, for $1 \leq i \leq N$. The joint probability mass function (PMF) of the random vector $\boldsymbol{S}$ is given as:

$$\mathbb{P}(\boldsymbol{S} = \boldsymbol{s}) = \prod_{i:\boldsymbol{s}(i)=\mathsf{LoS}} \mathsf{P}_{\mathsf{LoS}}(\boldsymbol{x}, \boldsymbol{x_i}) \times \prod_{j:\boldsymbol{s}(j)=\mathsf{NLoS}} (1 - \mathsf{P}_{\mathsf{LoS}}(\boldsymbol{x}, \boldsymbol{x_j})) \ , \quad (20)$$

where $\mathsf{P}_{\mathsf{LoS}}(\boldsymbol{x}, \boldsymbol{x_i})$ is obtained from (4). Next we define an indicator random variable, $\mathbb{I}_{\mathsf{N}} : \Omega \rightarrow \{0, 1\}$, associated with the occurrence of the NLoS state as:

$$\mathbb{I}_{\mathsf{N}}(\mathsf{S}_{\mathsf{A,i}}) = \begin{cases} 1, & \text{if } \mathsf{S}_{\mathsf{A,i}} = \mathsf{NLoS} \\ 0, & \text{if } \mathsf{S}_{\mathsf{A,i}} = \mathsf{LoS} \end{cases} . \quad (21)$$

In other words, the indicator random variable has a value 1 if the NLoS event occurs and has value 0 otherwise.

$$\hat{\tau}_{ij} \sim \begin{cases} \mathcal{N}\left(\frac{d_i-d_j}{c}, \eta^{\mathsf{NLoS}}(\sigma_i^2+\sigma_j^2)+2\sigma_{\mathsf{b}}^2\right), & \text{with } (1-\mathsf{P}_{\mathsf{LoS}}(\boldsymbol{x},\boldsymbol{x_i}))(1-\mathsf{P}_{\mathsf{LoS}}(\boldsymbol{x},\boldsymbol{x_j})) \\ \mathcal{N}\left(\frac{d_i-d_j}{c}-\mu_{\mathsf{b}}, \eta^{\mathsf{LoS}}\sigma_i^2+\eta^{\mathsf{NLoS}}\sigma_j^2+\sigma_{\mathsf{b}}^2\right), & \text{with } (1-\mathsf{P}_{\mathsf{LoS}}(\boldsymbol{x},\boldsymbol{x_j}))\mathsf{P}_{\mathsf{LoS}}(\boldsymbol{x},\boldsymbol{x_i}) \\ \mathcal{N}\left(\frac{d_i-d_j}{c}+\mu_{\mathsf{b}}, \eta^{\mathsf{NLoS}}\sigma_i^2+\eta^{\mathsf{LoS}}\sigma_j^2+\sigma_{\mathsf{b}}^2\right), & \text{with } (1-\mathsf{P}_{\mathsf{LoS}}(\boldsymbol{x},\boldsymbol{x_i}))\mathsf{P}_{\mathsf{LoS}}(\boldsymbol{x},\boldsymbol{x_j}) \\ \mathcal{N}\left(\frac{d_i-d_j}{c}, \eta^{\mathsf{LoS}}(\sigma_i^2+\sigma_j^2)\right), & \text{with } \mathsf{P}_{\mathsf{LoS}}(\boldsymbol{x},\boldsymbol{x_i})\mathsf{P}_{\mathsf{LoS}}(\boldsymbol{x},\boldsymbol{x_j}) \end{cases} . \tag{19}$$

Lemma 3: For a given realization of $\boldsymbol{S}=\boldsymbol{s}$, the *conditional distribution* of the TDOA *measurement vector*, $\boldsymbol{z}$, has a joint-Gaussian distribution $\boldsymbol{z} \sim \mathcal{N}\left(\boldsymbol{\mu}\left(\mathbf{x},\boldsymbol{s}\right), \boldsymbol{R}\left(\mathbf{x},\boldsymbol{s}\right)\right)$, where the i^{th} element of the mean vector, $\boldsymbol{\mu}\left(\mathbf{x},\boldsymbol{s}\right) \in \mathbb{R}^{(N-1)\times 1}$, $\boldsymbol{\mu}(i)$ and the (k,j)-element of the co-variance matrix $\boldsymbol{R}\left(\mathbf{x},\boldsymbol{s}\right) \in \mathbb{R}^{(N-1)\times(N-1)}$, $\boldsymbol{R}(k,j)$, for $1 \le i \le N-1$ and $1 \le j \le N-1$, are given in (22) and (23), respectively.

Proof: See Appendix C. ∎

Lemma 4: The marginal probability density function, $p\left(\boldsymbol{z}|\boldsymbol{x}\right)$, of the jointly-Gaussian distributed TDOA measurement vector $\boldsymbol{z} = [\hat{\tau}_{12}, \hat{\tau}_{13}...\hat{\tau}_{1N}]$, for a given UAV location (x,y,h) can be computed as:

$$p\left(\boldsymbol{z}|\boldsymbol{x}\right) = \sum_{\boldsymbol{s}\in\{\mathsf{LoS},\mathsf{NLoS}\}^N} \mathbb{P}(\boldsymbol{S}=\boldsymbol{s}) p\left(\boldsymbol{z}|\boldsymbol{x},\boldsymbol{s}\right) ,$$
$$p\left(\boldsymbol{z}|\boldsymbol{x},\boldsymbol{s}\right) = \frac{e^{\left(-\frac{1}{2}(\boldsymbol{z}-\boldsymbol{\mu}(\boldsymbol{x},\boldsymbol{s}))^T \boldsymbol{R}^{-1}(\boldsymbol{x},\boldsymbol{s})(\boldsymbol{z}-\boldsymbol{\mu}(\boldsymbol{x},\boldsymbol{s}))\right)}}{\sqrt{2\pi|\boldsymbol{R}\left(\boldsymbol{x},\boldsymbol{s}\right)|}} , \tag{24}$$

where the probability value, $\mathbb{P}(\boldsymbol{S}=\boldsymbol{s})$, is obtained from (20) and $\mu\left(\boldsymbol{x},\boldsymbol{s}\right)$ and $\boldsymbol{R}\left(\boldsymbol{x},\boldsymbol{s}\right)$ are formed using (22) and (23), respectively.

Proof: From (24) and (20), $\int_{\mathbb{R}^{N-1}} p\left(\boldsymbol{z}|\boldsymbol{x}\right) \ \boldsymbol{dz} = \sum_{\boldsymbol{s}} \mathbb{P}(\boldsymbol{S}=\boldsymbol{s}) \int_{\mathbb{R}^{N-1}} p\left(\boldsymbol{z}|\boldsymbol{x},\boldsymbol{s}\right) \ \boldsymbol{dz} = 1$, and therefore the likelihood function also satisfies the regularity condition: $\mathbb{E}\left[\frac{\partial \log p(\boldsymbol{z}|\boldsymbol{x})}{\partial x_j}\right] = 0$, for $1 \le j \le 3$. ∎

VI. TDOA-Based Localization and CRLB

In this section we formulate the TDOA-based MLE estimator for the 3D localization. Given (22) and (23), we realize that the likelihood function for the TDOA measurement vector, $\boldsymbol{z}$, is a function of the UAV location $\boldsymbol{x}=(x,y,h)$ and the ML estimate of $\boldsymbol{x}$ is given as:

$$\hat{\boldsymbol{x}} = \arg\max_{\boldsymbol{x}} \ \ p\left(\boldsymbol{z}|\boldsymbol{x}\right) \ . \tag{25}$$

The relationship between the mean square error (MSE) and the Fisher information matrix (FIM), $I_{\hat{\boldsymbol{x}}}$ can be given as [40]:

$$E(x,y,h) \ge \text{trace}[\boldsymbol{I}^{-1}(x,y,h)] \ , \tag{26}$$

where the inverse of the FIM is the CRLB on the covariance matrix of the location estimates given as: $\boldsymbol{c_{\hat{x}}} - \boldsymbol{I_{\hat{x}}^{-1}} \ge \boldsymbol{0}$. Next we provide the expressions for each element of the FIM, across various scenarios discussed in this paper.

Theorem 1: For a network of N synchronized ground sensors located in a mixed LoS/NLoS environment, the (i,j) element of the FIM, for $1 \le i,j \le 3$, is given as:

$$I_{ij} = -\mathbb{E}_{\boldsymbol{Z}}\left[\frac{1}{p^2\left(\boldsymbol{z}|\boldsymbol{x}\right)} \frac{\partial p\left(\boldsymbol{z}|\boldsymbol{x}\right)}{\partial x_i} \frac{\partial p\left(\boldsymbol{z}|\boldsymbol{x}\right)}{\partial x_j}\right] , \tag{27}$$

where the partial derivative of the conditional density function, $p(\boldsymbol{z}|\boldsymbol{x})$ with respect to each location coordinate x_i is given in (29), where $\frac{\partial \mathbb{P}(\boldsymbol{S}=\boldsymbol{s})}{\partial x_i}$, the partial derivative of the joint probability of the N FTs being in LoS/NLoS states, $\mathbb{P}(\boldsymbol{S}=\boldsymbol{s})$, with respect to x_i is given as:

$$\frac{\partial \mathbb{P}(\boldsymbol{S}=\boldsymbol{s})}{\partial x_i} = \sum_{m:\boldsymbol{s}(m)=\mathsf{LoS}} \frac{\mathbb{P}(\boldsymbol{S}=\boldsymbol{s})}{\mathsf{P}_{\mathsf{LoS}}(\boldsymbol{x},\boldsymbol{x_m})} \frac{\partial \mathsf{P}_{\mathsf{LoS}}(\boldsymbol{x},\boldsymbol{x_m})}{\partial x_i} - \sum_{n:\boldsymbol{s}(n)=\mathsf{NLoS}} \frac{\mathbb{P}(\boldsymbol{S}=\boldsymbol{s})}{1-\mathsf{P}_{\mathsf{LoS}}(\boldsymbol{x},\boldsymbol{x_n})} \frac{\partial \mathsf{P}_{\mathsf{LoS}}(\boldsymbol{x},\boldsymbol{x_n})}{\partial x_i} , \tag{28}$$

where $\frac{\partial \mathsf{P}_{\mathsf{LoS}}(\boldsymbol{x},\boldsymbol{x_m})}{\partial x_k} = c' \mathsf{P}_{\mathsf{LoS}}(\boldsymbol{x},\boldsymbol{x_m})(1-\mathsf{P}_{\mathsf{LoS}}(\boldsymbol{x},\boldsymbol{x_m})) \frac{\partial}{\partial x_k}\left(\frac{h}{r_m}\right)$, and $c' = \left(\frac{-180ab\mathsf{P}_{\mathsf{LoS}}}{\pi}\right)$.

Proof: See Appendix D. ∎

From (27), we see that computing the required FIM elements involves working with the conditional pdf $p(\boldsymbol{z}|\boldsymbol{x},\boldsymbol{s})$ for a given realization of the random vector $\boldsymbol{S}=\boldsymbol{s}$. Thus, we approximate the true expectation in (27) by generating a large number of samples of the random vector $\boldsymbol{z}$, using the respective distributions given in (22), (23), for each possible realization of $\boldsymbol{S}$, out of all the 2^N cases mentioned in (20). Finally, we take the average of all the values of the term $\frac{1}{p^2(\boldsymbol{z}|\boldsymbol{x})} \frac{\partial p(\boldsymbol{z}|\boldsymbol{x})}{\partial x_i} \frac{\partial p(\boldsymbol{z}|\boldsymbol{x})}{\partial x_j}$, using (28) and (29), for all the said samples of $\boldsymbol{z}$. The general expressions for the elements of the FIM for the special case of a purely LoS environment, is presented as a corollary (corollary 1) to Theorem 1.

Corollary 1: In a purely LoS environment, the (i,j) element of the FIM [40], for $1 \le i,j \le 3$, is given in (30). This follows from noticing $p\left(\boldsymbol{z}|\boldsymbol{x}\right) = p\left(\boldsymbol{z}|\boldsymbol{x},\boldsymbol{s}\right)$, where $\boldsymbol{s}(k) = \mathsf{LoS}$, for $1 \le k \le N$.

Next we derive the elements of the FIM for the various antenna patterns in a purely LoS environment. Since the mean vector of the TDOA measurement $\boldsymbol{\mu}(\boldsymbol{x})$ does not change with varying antenna patterns, we only provide the expressions for $\frac{\partial \sigma_j^2}{\partial x_i}$, for an arbitrary j ($1 \le j \le 3$), for the three different antenna orientations, namely, $\frac{\partial \sigma_{\text{j-VV}}^2}{\partial x_i}$, $\frac{\partial \sigma_{\text{j-HH}}^2}{\partial x_i}$, and $\frac{\partial \sigma_{\text{j-VH}}^2}{\partial x_i}$, as this is sufficient to compute the $\frac{\partial \boldsymbol{R}}{\partial x_i}$ term using (31). Since $\frac{\partial \sigma_{\text{j-VH}}^2}{\partial x_i}$, can be decomposed in terms of $\frac{\partial \sigma_{\text{j-VV}}^2}{\partial x_i}$ and $\frac{\partial \sigma_{\text{j-HH}}^2}{\partial x_i}$, in the corollaries below, we provide the relationship between $\frac{\partial \sigma_{\text{j-VH}}^2}{\partial x_i}$, $\frac{\partial \sigma_{\text{j-VV}}^2}{\partial x_i}$, and $\frac{\partial \sigma_{\text{j-HH}}^2}{\partial x_i}$, and the expression for $\frac{\partial \sigma_{\text{j-VH}}^2}{\partial x_i}$, for the two cases: the realistic half-wave dipole antenna pattern and the approximated dipole antenna pattern. In the case of the VV antenna orientation, for $1 \le i \le N$ and $1 \le j \le 3$, the term $\frac{\partial \sigma_{\text{i-VH}}^2}{\partial x_j}$, can be expressed in terms of $\frac{\partial \sigma_{\text{j-VV}}^2}{\partial x_i}$ and $\frac{\partial \sigma_{\text{j-HH}}^2}{\partial x_i}$ as:

$$\frac{\partial \sigma_{\text{i-VH}}^2}{\partial x} = -\frac{1}{2}\left(\frac{\sigma_{\text{i-HH}}}{\sigma_{\text{i-VV}}^3} \frac{\partial \sigma_{\text{i-VV}}^2}{\partial x} + \frac{\sigma_{\text{i-VV}}}{\sigma_{\text{i-HH}}^3} \frac{\partial \sigma_{\text{i-HH}}^2}{\partial x}\right) . \tag{32}$$

$$\boldsymbol{\mu}(i) = \frac{(d_1 - d_{i+1})}{c} + \mu_b \Big[\mathbb{I}_{\mathsf{N}}(\mathsf{S}_{\mathsf{A},1}) - \mathbb{I}_{\mathsf{N}}(\mathsf{S}_{\mathsf{A},\mathsf{i}+1}) \Big] \ , \tag{22}$$

$$\boldsymbol{R}(i,j) = \begin{cases} \sigma_{\mathsf{b}}^2 \Big[\mathbb{I}_{\mathsf{N}}(\mathsf{S}_{\mathsf{A},1}) + \mathbb{I}_{\mathsf{N}}(\mathsf{S}_{\mathsf{A},\mathsf{i}+1}) \Big] + \eta^{\mathsf{NLoS}} \Big[\mathbb{I}_{\mathsf{N}}(\mathsf{S}_{\mathsf{A},1}) \sigma_1^2 + \mathbb{I}_{\mathsf{N}}(\mathsf{S}_{\mathsf{A},\mathsf{i}+1}) \sigma_{i+1}^2 \Big] \\ \qquad + \eta^{\mathsf{LoS}} \Big[\big(1 - \mathbb{I}_{\mathsf{N}}(\mathsf{S}_{\mathsf{A},1})\big) \sigma_1^2 + \big(1 - \mathbb{I}_{\mathsf{N}}(\mathsf{S}_{\mathsf{A},\mathsf{i}+1})\big) \sigma_{i+1}^2 \Big] \ , \qquad i = j \ . \\ \sigma_{\mathsf{b}}^2 \mathbb{I}_{\mathsf{N}}(\mathsf{S}_{\mathsf{A},1}) + \eta^{\mathsf{NLoS}} \Big[\mathbb{I}_{\mathsf{N}}(\mathsf{S}_{\mathsf{A},1}) \sigma_1^2 \Big] + \eta^{\mathsf{LoS}} \Big[\big(1 - \mathbb{I}_{\mathsf{N}}(\mathsf{S}_{\mathsf{A},1})\big) \sigma_1^2 \Big] \ , \qquad i \neq j \end{cases} \tag{23}$$

$$\frac{\partial p(\boldsymbol{z}|\boldsymbol{x})}{\partial x_i} = \sum_s p\left(\boldsymbol{z}|\boldsymbol{x},\boldsymbol{s}\right) \left[\frac{\partial \mathbb{P}(\boldsymbol{S}=\boldsymbol{s})}{\partial x_i} - \frac{1}{2} \mathbb{P}(\boldsymbol{S}=\boldsymbol{s}) \sqrt{|\boldsymbol{R}(\boldsymbol{x},\boldsymbol{s})|} \ \mathrm{Tr}\left(\boldsymbol{R}^{-1}(\boldsymbol{x},\boldsymbol{s}) \frac{\partial R^T(\boldsymbol{x},\boldsymbol{s})}{\partial x_i} \right) \right] +$$

$$\sum_s \mathbb{P}(\boldsymbol{S}=\boldsymbol{s}) p\left(\boldsymbol{z}|\boldsymbol{x},\boldsymbol{s}\right) \left[\frac{\partial \boldsymbol{\mu}^T(\boldsymbol{x},\boldsymbol{s})}{\partial x_i} \boldsymbol{R}^{-1}(\boldsymbol{x},\boldsymbol{s}) \big(\boldsymbol{z} - \mu(\boldsymbol{x},\boldsymbol{s})\big) - \frac{1}{2} \big(\boldsymbol{z} - \mu(\boldsymbol{x},\boldsymbol{s})\big)^T \frac{\partial \boldsymbol{R}^{-1}(\boldsymbol{x},\boldsymbol{s})}{\partial x_i} \big(\boldsymbol{z} - \mu(\boldsymbol{x},\boldsymbol{s})\big) \right] \ , \tag{29}$$

$$I_{ij} = \frac{\partial \boldsymbol{\mu}(\boldsymbol{x})}{\partial x_i} \boldsymbol{R}^{-1}(\boldsymbol{x}) \frac{\partial \boldsymbol{\mu}(\boldsymbol{x})}{\partial x_i}^T + \frac{1}{2} \mathrm{trace} \left(\boldsymbol{R}^{-1}(\boldsymbol{x}) \frac{\partial \boldsymbol{R}(\boldsymbol{x})}{\partial x_i} \boldsymbol{R}^{-1}(\boldsymbol{x}) \frac{\partial \boldsymbol{R}(\boldsymbol{x})}{\partial x_j} \right) \ , \tag{30}$$

where for $1 \leq m \leq (N-1)$ and $1 \leq m \leq (N-1)$,

$$\frac{\partial \boldsymbol{\mu}}{\partial x_i}(k) = \frac{1}{c} \left(\frac{\partial d_1}{\partial x_i} - \frac{\partial d_{k+1}}{\partial x_i} \right) \ , \quad \frac{\partial \boldsymbol{R}}{\partial x_i}(k,m) = \frac{\partial \sigma_1^2}{\partial x_i} + \frac{\partial \sigma_{k+1}^2}{\partial x_i} \ , \quad \frac{\partial \boldsymbol{R}}{\partial x_i}(k,k) = \frac{\partial \sigma_1^2}{\partial x_i} \ . \tag{31}$$

Corollary 2: For a half-wave dipole antenna pattern, and $1 \leq i \leq N$ and $1 \leq j \leq 3$, the term $\frac{\partial \sigma^2_{\text{i-VV}}}{\partial x_j}$ is given as:

$$\frac{\partial \sigma^2_{\text{i-VV}}}{\partial x} = \frac{2\left(x - x_i\right)\left(1 - \pi k {d_i}^{-3} h {r_i}^2 \tan\left(\beta\right)\right)}{\cos^2\left(\beta\right)} \ ,$$
$$\frac{\partial \sigma^2_{\text{i-VV}}}{\partial y} = \frac{2\left(y - y_i\right)\left(1 - \pi k {d_i}^{-3} h {r_i}^2 \tan\left(\beta\right)\right)}{\cos^2\left(\beta\right)},$$
$$\frac{\partial \sigma^2_{\text{i-VV}}}{\partial h} = \frac{2\pi k {d_i}^{-3} {r_i}^4 \tan\left(\beta\right)}{\cos^2\left(\beta\right)} \ , \tag{33}$$

where $\beta = \frac{\pi k h}{d_i}$, and the term $\frac{\partial \sigma^2_{\text{i-HH}}}{\partial x_j}$ is given as:

$$\frac{\partial \sigma^2_{\text{i-HH}}}{\partial x} = \frac{2\left(x - x_i\right)\left(1 - \pi k {d_i}^{-3} \left(y - y_i\right) \psi_i(x,h) \tan\theta\right)}{\cos^2\theta} \ ,$$
$$\frac{\partial \sigma^2_{\text{i-HH}}}{\partial h} = \frac{2h\left(1 - \pi k {d_i}^{-3} \psi_i(x,h) \left(y - y_i\right) \tan\theta\right)}{\cos^2\theta} \ ,$$
$$\frac{\partial \sigma^2_{\text{i-HH}}}{\partial y} = \frac{2\pi k {d_i}^{-3} \left(\psi_i(x,h)\right)^2 \tan\theta}{\cos^2\theta}, \tag{34}$$

where $\theta = \frac{(y - y_i)}{d_i}$ and $\psi_i(x,h) = \left(x - x_i\right)^2 + h^2$.

Proof: See Appendix E. ∎

Corollary 3: In the case of the approximated antenna patterns, the expressions for $\frac{\partial \sigma^2_{\text{i-HH}}}{\partial x_j}$, with $1 \leq i \leq N$ and $1 \leq j \leq 3$, are given as:

$$\frac{\partial \sigma^2_{\text{i-HH}}}{\partial x} = \frac{4k(x - x_i){d_i}^2}{h^2} \ , \quad \frac{\partial \sigma^2_{\text{i-HH}}}{\partial y} = \frac{4k(y - y_i){d_i}^2}{h^2} \ ,$$
$$\frac{\partial \sigma^2_{\text{i-HH}}}{\partial h} = 2k \left(\frac{2{d_i}^2}{h} - \frac{{d_i}^4}{h^3} \right) \ , \tag{35}$$

whereas the $\frac{\partial \sigma^2_{\text{i-VV}}}{\partial x_j}$ terms are given as:

$$\frac{\partial \sigma^2_{\text{i-VV}}}{\partial h} = \frac{4khd_i^2}{{d_i}^2 - h^2} \ , \quad \frac{\partial \sigma^2_{\text{i-VV}}}{\partial y} = 2k(y - y_i)\Phi_i(x,y,h) \ ,$$
$$\frac{\partial \sigma^2_{\text{i-VV}}}{\partial x} = 2k(x - x_i)\Phi_i(x,y,h) \ , \tag{36}$$

where $\Phi_i(x,y,h) = {d_i}^2 \left(\frac{2}{{d_i}^2 - h^2} - \frac{{d_i}^2}{{d_i}^2 - h^2} \right)$.

Proof: See Appendix E. ∎

In the next corollary we compute the terms necessary for obtaining the FIM elements in the case of a multi-antenna sensor network in a purely LoS environment.

Corollary 4: The FIM elements for the V-HV and the H-HV patterns for the multi-antenna acquisition technique, are obtained in terms of $\frac{\partial \sigma^2_{\text{i-VV}}}{\partial x_j}$ and $\frac{\partial \sigma^2_{\text{i-HH}}}{\partial x_j}$, with $1 \leq i \leq N$ and $1 \leq j \leq 3$, are given as:

$$\frac{\partial \sigma^2_{\text{i,V-HV}}}{\partial x_j} = \frac{1}{2} \left(1 + \frac{\sigma^2_{\text{i-VV}}}{\sigma^2_{\text{i-HH}}} \right)^{-\frac{1}{2}} \left[\frac{\partial \sigma^2_{\text{i-VV}}}{\partial x_j} + \frac{\sigma^4_{\text{i-VV}} \sigma^2_{\text{i-HH}}}{\sigma^2_{\text{i-HH}} + \sigma^2_{\text{i-VV}}} \Psi(i.j) \right] \ ,$$
$$\frac{\partial \sigma^2_{\text{i,H-HV}}}{\partial x_j} = \frac{1}{2} \left(1 + \frac{\sigma^2_{\text{i-HH}}}{\sigma^2_{\text{i-VV}}} \right)^{-\frac{1}{2}} \left[\frac{\partial \sigma^2_{\text{i-HH}}}{\partial x_j} + \frac{\sigma^4_{\text{i-HH}} \sigma^2_{\text{i-VV}}}{\sigma^2_{\text{i-HH}} + \sigma^2_{\text{i-VV}}} \Psi(i,j) \right] \ . \tag{37}$$

where $\Psi(i.j) = \sigma^{-4}_{\text{i-HH}} \frac{\partial \sigma^2_{\text{i-HH}}}{\partial x_j} + \sigma^{-4}_{\text{i-VV}} \frac{\partial \sigma^2_{\text{i-VV}}}{\partial x_j}$.

Proof: See Appendix F. ∎

VII. Numerical Results

In this section, we present numerical results that illustrate the impact of the various antenna orientations on the performance of the TDOA-based localization scheme for the dipole antenna models in Table II. All the plots in this sections are drawn using the CRLB expressions derived in Section VI.

A. System Assumptions and Parameters

We consider an area of size $1000 \times 1000\,\mathrm{m}^2$ with 4 RF sensors placed at the following 2D coordinates: $\boldsymbol{x_1} =$

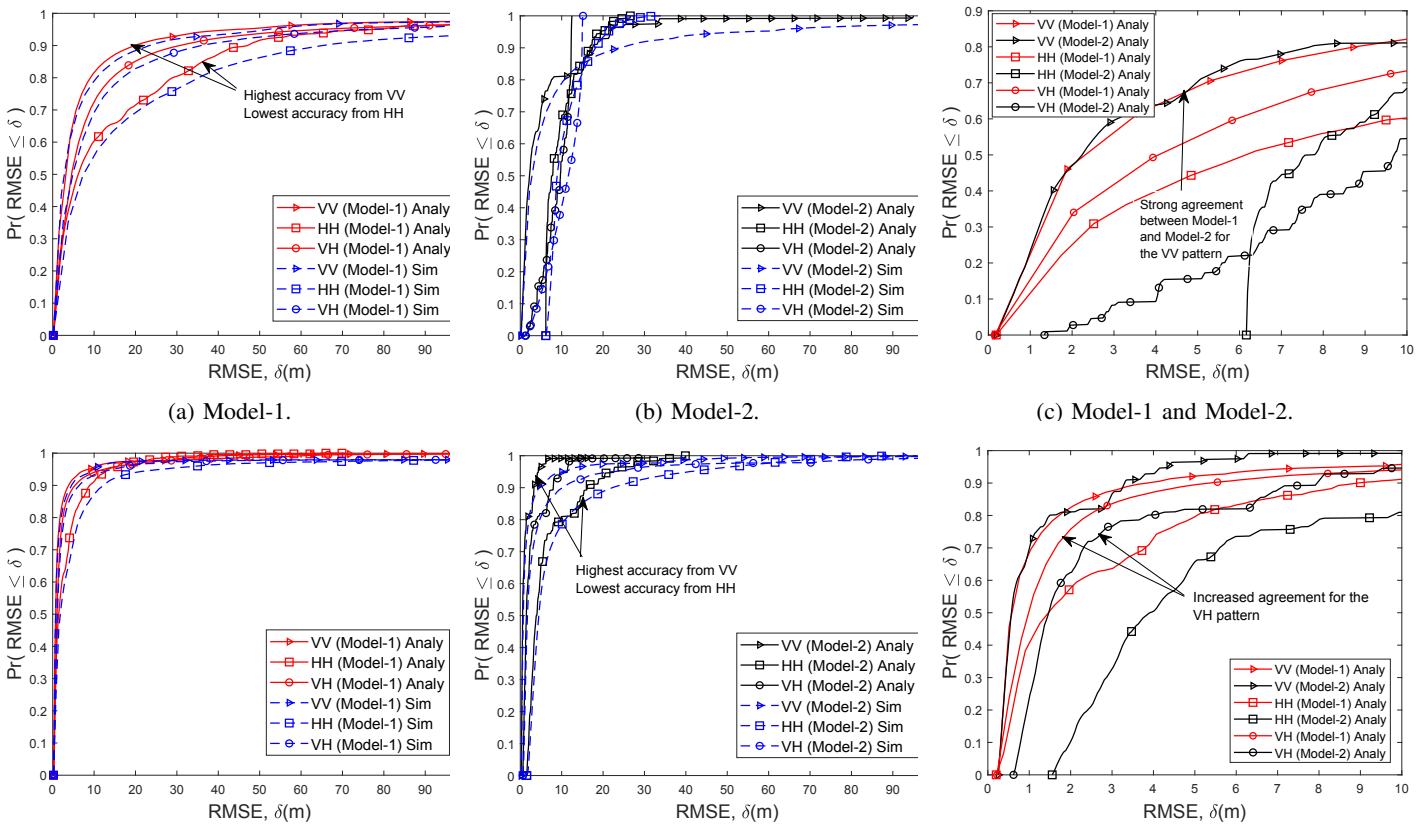

(a) Model-1. (b) Model-2. (c) Model-1 and Model-2.

(d) Model-1. (e) Model-2. (f) Model-1 and Model-2.

Fig. 4: CRLB RMSE distribution for single receive antenna for VV, VH, and HH orientations of the two antenna patterns (Model-1 and Model-2) at UAV altitudes of (a-c) 10 meters, and (d-f) 100 meters.

$(250, 250)$ m, $\boldsymbol{x_2} = (-250, 250)$ m, $\boldsymbol{x_3} = (-250, -250)$ m, and $\boldsymbol{x_4} = (250, -250)$ m. We also assume that the bandwidth and the transmit power of the UAV are 10 MHz and 20 dBm, respectively [4], [5], and that the noise power spectral density (PSD) is -174 dBm/Hz [44]. In order to demonstrate the difference in the localization performance caused by a mixed LoS/NLoS A2G channel as compared to a purely LoS channel, we plot the localization error in a suburban and an urban environment, where the two A2G channels are characterized by (3) and (4), with the following set of parameters: $(a, b) = (4.88, 0.429)$, $(\eta^{\mathsf{LoS}}, \eta^{\mathsf{NLoS}}) = (0.1, 21)$ dB for the suburban setting, and $(a, b) = (9.6117, 0.1581)$, $(\eta^{\mathsf{LoS}}, \eta^{\mathsf{NLoS}}) = (1, 20)$ dB for the urban setting [36]. Lastly, for the results related to the Model-1 antenna pattern, we consider a half-wave dipole antenna, where $l = \frac{\lambda}{2}$.

For all the plots in Figs. 4, 5, 8, 9, in addition to theoretical results, we also provide simulation results for a gradient-decent based location estimator. The process of the simulation is as follows. We consider a uniform grid over our 1 km $\times$ 1 km system area, and each node of the grid is considered for the unknown UAV location ($\boldsymbol{x} = (x, y, h)$). For $1 \leq i \leq 4$, for all combinations of $\boldsymbol{x_i}$ and $\boldsymbol{x}$, TOA measurements, $\hat{\tau}_i$, are generated by generating 4 random numbers, each drawn from Gaussian distributions described by (8) in the purely LoS case, and by (17), in the case of a mixed LoS/NLoS scenario. These TOA measurements are then used to generate the TDOA measurements: $\hat{\tau}_{12}, \hat{\tau}_{13}, \hat{\tau}_{14}$, according to (18). Finally we construct the marginal probability density function, $p(\boldsymbol{z}|\boldsymbol{x})$, of the jointly-Gaussian distributed TDOA measurement vector $\boldsymbol{z} = [\hat{\tau}_{12}, \hat{\tau}_{13}, \hat{\tau}_{14}]$ using (24), for a given UAV location (x, y, h). Following (25), the location estimate $\hat{\boldsymbol{x}}$, of the unknown UAV location is then obtained by maximizing nonlinear likelihood function with help of a method of gradient descent [45]. Since the likelihood function is highly nonlinear and complicated, we find the best approximation to the solution by randomly choosing an initial solution and then performing a fixed large number (5000) of iterations of iterations of the gradient descent method. We repeat the same process of simulation for the different altitudes and antenna patterns to produce the results on the localization error, $||\boldsymbol{x} - \hat{\boldsymbol{x}}||_{\mathbb{R}^3}$, as presented in Fig. 4, Fig. 5, Fig. 8, and Fig. 9.

B. Single Antenna Localization in LoS Channel

In Fig. 4 and Fig. 5, we characterize the theoretical and simulated localization performance provided by the different SISO antenna orientations (i.e. VV, VH, and HH) in a purely LoS environment, across various UAV altitudes ranging from 10 meters to 700 meters. While the first two columns in each row of Fig. 4, and Fig. 5, describe the localization CRLB and the gradient-descent based localization error for Model-1 and

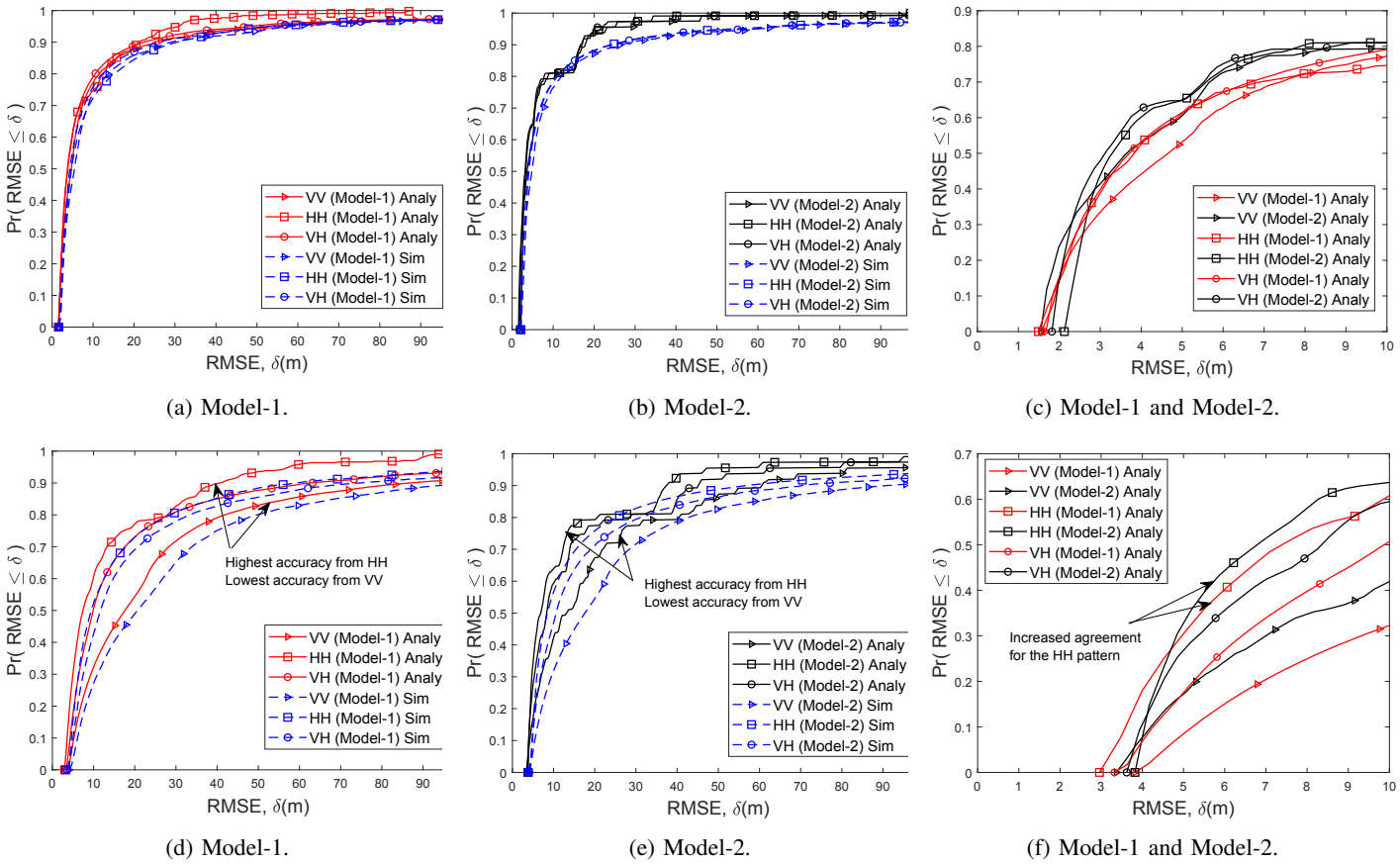

(a) Model-1. (b) Model-2. (c) Model-1 and Model-2.

(d) Model-1. (e) Model-2. (f) Model-1 and Model-2.

Fig. 5: CRLB RMSE distribution for single receive antenna for VV, VH, and HH orientations of the two antenna patterns (Model-1 and Model-2) at UAV altitudes of (a-c) 500 meters, and (d-f) 700 meters.

Model-2, respectively, the third column depicts the agreement between the two antenna pattern models at the low localization error region.

As demonstrated by Fig. 4(a), we observe that at very low UAV altitudes, such as 10 meters, the CDF for the VV (Model-1) pattern lies above the VH and HH patterns (for Model-1), for all values of the localization RMSE, δ. This implies that, at the very low altitudes, the best localization coverage Pr(RMSE $\leq \delta$), for the Model-1 pattern, is provided by the VV pattern, followed by the VH and the HH patterns. On the contrary the curves in Fig. 4(b), show us that, although the VV orientation among the Model-2 antenna patterns achieves the highest coverage probability subject to very low error tolerances (such as $\delta \leq 10$ m), the best coverage probability for relatively higher error tolerances ($\delta \geq 10$ m), is provided by the Model-2 VV pattern. From Fig. 4(c), we also note that at very low altitudes the Model-2 antenna patterns find the best agreement with the Model-1 antenna patterns, for the VV orientation but there is a non-negligible performance gap between the two models for the VH and the HH orientations.

Next, from Fig. 4(d) and Fig. 4(e), we observe that for medium UAV altitudes of about 100 meters, the VV orientation yields the highest area coverage probability subject to all values of the RMSE threshold, followed by the VH and the HH orientations, for both the Model-1, and Model-2 antenna patterns. In addition, from Fig. 4(f), we note that, at medium altitudes there is a strong agreement between Model-1, and Model-2 with respect to the VV orientation, followed by the VH and the HH orientation. On the contrary, Fig. 5(a) through Fig. 5(c), illustrate that, at an altitude of 500 meters, the CDF curves for all the orientations almost overlap with each other, for both Model-1, and Model-2.

Most interestingly, from Fig. 5(d), and Fig. 5(e), we see that, at an even higher altitude of 700 meters, the HH orientation yields the highest coverage probability, followed by the VH and the VV orientations, for both Model-1, and Model-2. This particular result lies in complete contrast with our earlier observation for the lower altitudes of 10 meters, and 100 meters, where the highest and the lowest coverage probability was produced by the VV and the HH orientation, respectively. Finally, we observe that the CRLBs provide a reasonably tight lower bound on the localization errors produced by the gradient descent-based location estimators (simulation results) across all antenna orientations and all drone altitudes.

Having realized how the performance of the different orientations changes with the UAV altitude, we plot the median RMSE as a function of the UAV altitude for both the Model-1 and Model-2 antenna patterns, respectively, in Fig. 6(a) and Fig. 6(b). The curves in Fig. 6 illustrate that the localization accuracy for both the Model-1 and Model-2 antenna pattern

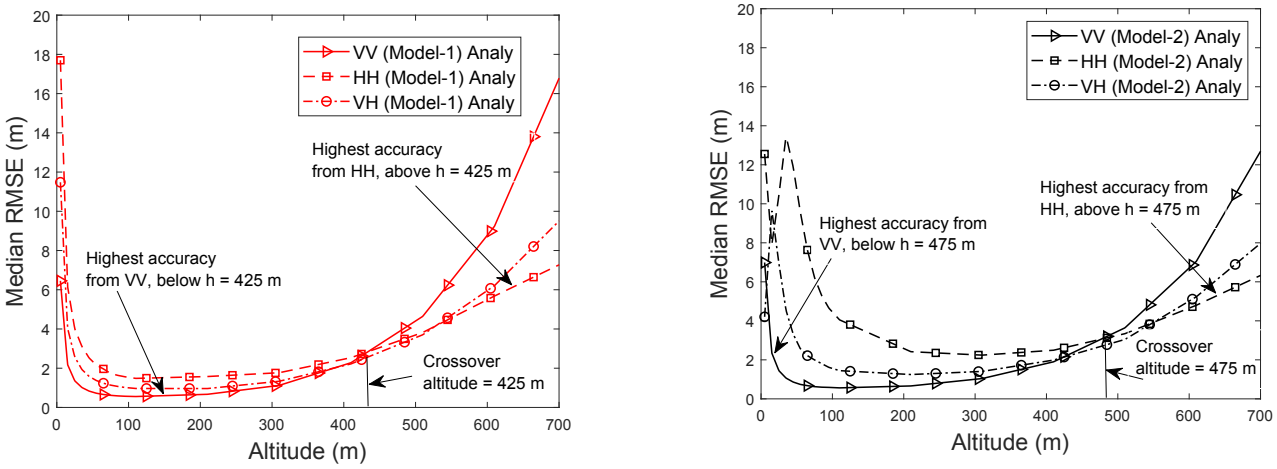

(a) Antenna pattern: Model-1.

(b) Antenna pattern: Model-2.

Fig. 6: Median RMSE as functions of UAV altitude for the various orientations (VV, VH and HH) of (a) realistic, and (b) approximated dipole antenna pattern.

change in a non-monotonic pattern with respect to the UAV altitude, and that there exist respective critical heights where the corresponding median RMSE for the given antenna orientation is minimized. We also see that there exist points of intersection between the RMSE curves for the various antenna orientations, and the abscissa of the points of intersection of all the 3 curves gives us the crossover height beyond which the choice of the best antenna orientation changes. For example, Fig. 6(a), and Fig. 6(b) illustrate that the crossover altitude is, respectively, 425 meters, and 475 meters, for Model-1, and Model-2, below which the lowest median RMSE is obtained from the VV orientation, but beyond it, the best accuracy is achieved by the 'HH' orientation.

C. Multi Antenna Localization in LoS Channel

Next in Fig. 7, we demonstrate the improved robustness of the multi-antenna signal acquisition technique (described in Section IV-A1), to the mismatches in the antenna orientations arising from the single antenna techniques. Unlike the plots in the earlier figures, all the plots in Fig. 7 and on-wards discuss the localization performance only for the Model-1 antenna pattern, and does not include the curves corresponding to the Model-2 patterns. In particular, in Fig. 7, we consider Model-1 antenna pattern and compare the CDFs of the CRLB RMSE for the SISO (VV and HH) orientations, to the MISO orientations (V-HV and H-HV).

First of all we note that at all altitudes, the V-HV and the H-HV patterns yield higher coverage probability subject to all RMSE tolerance, δ m, as compared to the VV and the HH orientations, respectively. Next, from Fig. 7(b) and Fig. 7(c) we see that the red curves almost overlap with the corresponding black curves, which in turn indicates that at the medium altitudes (i.e. between 100 meters to 500 meters) the gain in the accuracy is very small for both the MISO orientations. On the other hand Fig. 7(a) and Fig. 7(d) show us that at very low and very high altitudes (such as 10 meters and 700 meters), there is moderate to major gain due to using MISO orientations. In particular, from Fig. 7(a), we see that at very low altitudes, the MISO scheme has a considerable gain over the SISO scheme, HH, but only a marginal gain over VV. On the contrary, Fig. 7(d) shows us that at very high altitudes, the MISO localization gain is high over the VV orientation, but small over the HH orientation.

D. Localization Performance in Mixed LoS/NLoS Environment

Due to the introduction of a positive bias, the localization in a mixed LoS/NLoS environment always experiences a performance loss, regardless of the antenna orientation in question. Therefore we choose to characterize the impact of the LoS/NLoS propagation, using a MISO orientation that provides an upper bound on all other antenna orientations, discussed in this paper. In particular, in Fig. 8, we plot the CDFs of the H-HV CRLB-RMSE, across various altitudes, in a suburban and an urban environment. As illustrated by Fig. 8(a) and Fig. 8(b), we note that, for lower to moderately high UAV altitudes, the localization errors in the suburban environment is lower than that in the urban environment. Moreover, while at very low altitudes, there is only a minor increase in the localization error in an urban environment, at medium altitudes the localization in an urban environment undergoes a severe performance loss. Next, contrary to the common intuition, Fig. 8(c) and Fig. 8(d), reveal that at very high altitudes, the performance in the urban environment is better than that in the suburban environments. This is because, at a very high altitude, the probability of LoS propagation in the suburban environment is very close to one, but the probability of LoS in the urban environment still keeps growing larger with the increasing UAV altitude. Thus, while the TOA measurements in the suburban environment are almost bias free at such altitudes, the average bias in the TOA measurement in the urban environment keeps decreasing with the increasing altitude. Therefore, at a very high altitude, the likelihood of the TDOA

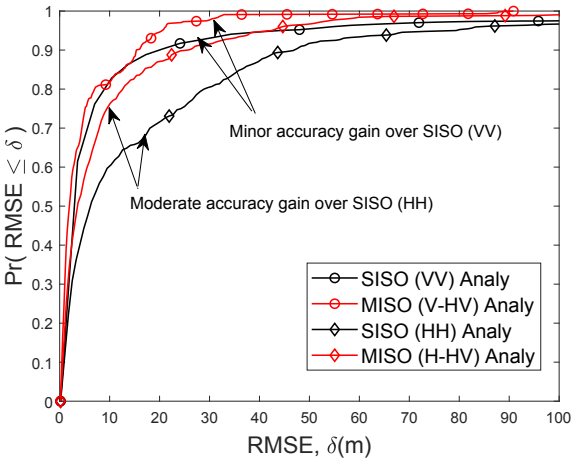

(a) UAV height: 10 meters.

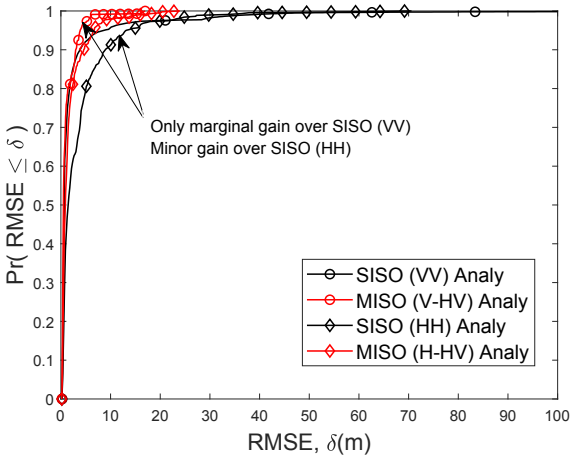

(b) UAV height: 100 meters.

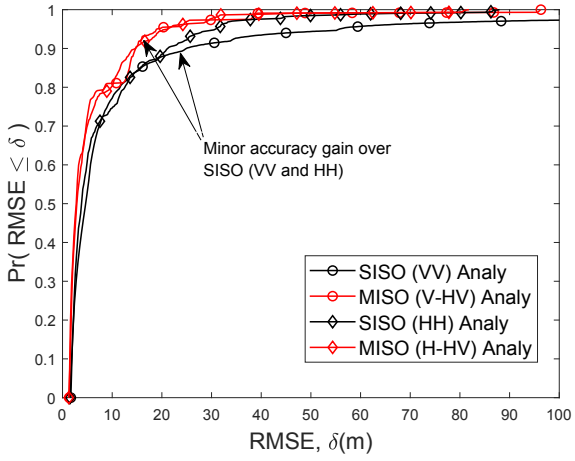

(c) UAV height: 500 meters.

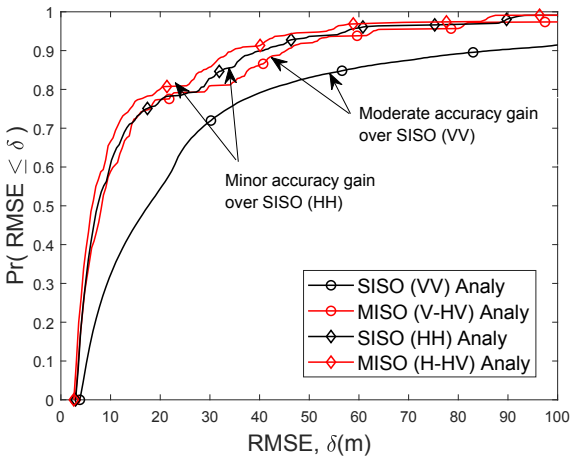

(d) UAV height: 700 meters.

Fig. 7: CRLB RMSE distribution for single and multiple dipole receive antennas with VV and HH orientations at UAV altitudes of (a) 10 meters, (b) 100 meters, (c) 500 meters, and (d) 700 meters.

measurements in the urban environment is more sensitive to the changes in the (x, y, z) coordinates, resulting in higher accuracy of the localization estimates. Simultaneously at such a high altitude, the SNR of the UAV signal is very low in both suburban and urban environments, and thus the variance of the LoS error in the TOA measurements is very high in both environments and not very sensitive to the changes in the environment anymore. Finally we note that the line curves in all the plots in Fig. 8, lies below the respective black and red curves with the markers, and closely follows them. This implies that the MISO CRLB provides a tight lower bound to the localization error of the gradient-descent based location estimator, across both the suburban and the urban environments, across all altitudes.

Next, in Fig. 9, we compare the dependence of the localization accuracy on the UAV altitude under different degrees of LoS dominance. From, Fig. 9(a) we note that the median RMSE changes in non-monotonic pattern, with respect to the UAV altitude, in both the suburban and the urban environment, and that the critical altitude (where the median localization error is minimized), in an urban environment (around 300 meters) is higher than that in a suburban environment (around 100 meters). In order to improve the resolution of the plot in Fig. 9(a), we plot the median RMSE against a shorter range of the UAV altitude, in Fig. 9(b). This allows us to note that the crossover altitude, where the localization error in the suburban environment increases beyond that in the urban environment is noted to be around 450 meters.

VIII. Conclusion

In this paper a TDOA-based RF positioning system for localization of UAVs is studied in conjunction with air-to-ground 3D antenna radiation patterns for dipole antennas. Our results show that accounting for antenna effects makes a significant difference and reveals many important relationships between the localization accuracy and the altitude of the UAV. We show that the localization performance varies in a non-monotonic pattern with respect to the UAV altitude. We are also able to characterize the critical heights at which the coverage and accuracy metrics are optimized, as well as the

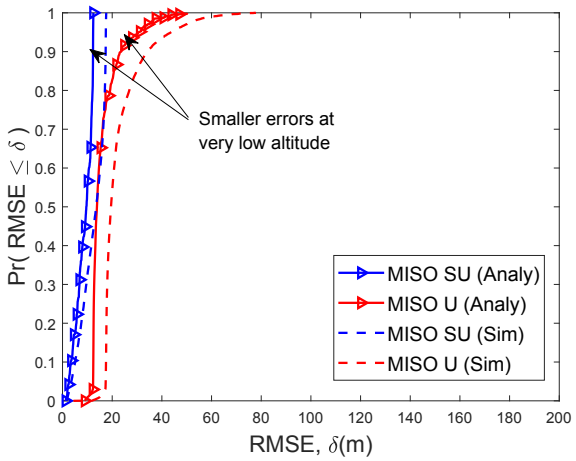

(a) UAV height: 10 meters.

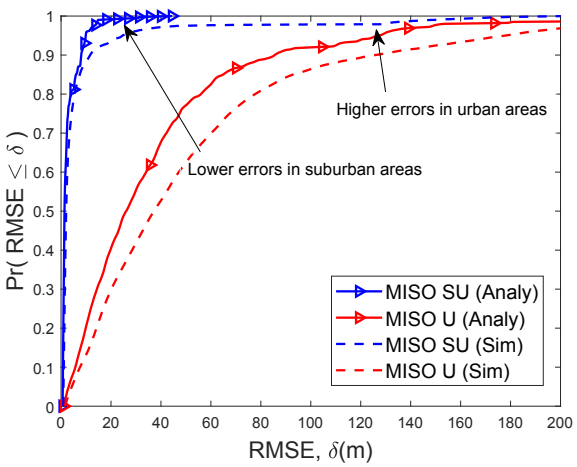

(b) UAV height: 100 meters.

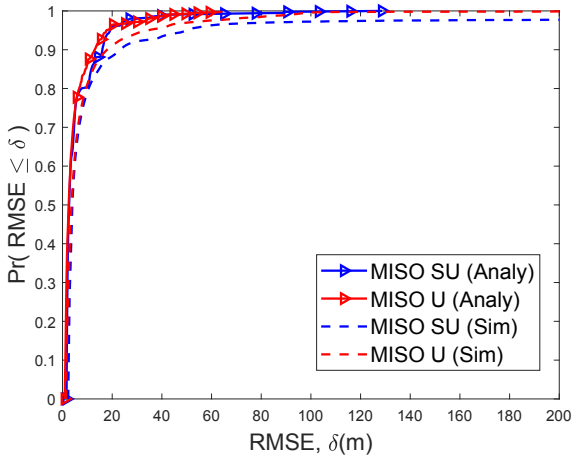

(c) UAV height: 500 meters.

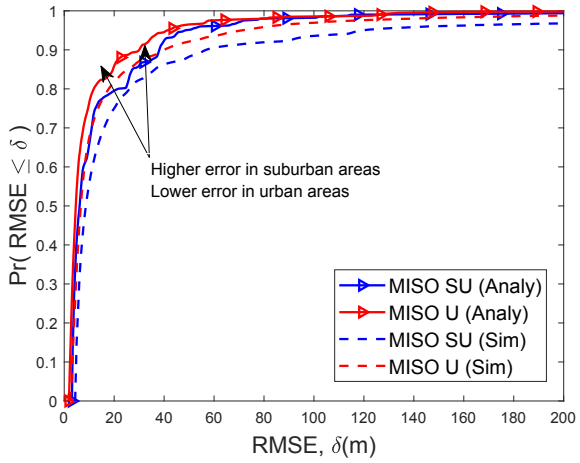

(d) UAV height: 700 meters.

Fig. 8: Impact of LoS/NLoS A2G link on CRLB RMSE Distribution for MISO receive antenna patterns at UAV altitudes of (a) 10 meters. (b) 100 meters, (c) 500 meters, and (b) 700 meters.

crossover UAV heights before and after which the choice of the best antenna pattern yielding best performance changes. This work has numerous possible extensions. Our framework can be extended to more complicated antenna pattern scenarios, such down-tilted sector antennas used by cellular base stations. The expressions for the lower bounds on the localization error derived in this study can be used to find the optimal location of the ground sensors with non-isotropic antenna patterns. Another meaningful extension would be to use this framework to investigate the selection of optimal reference sensor for TDOA observations in the presence of directional antenna patterns. Our future plans include doing experiments over the NSF AERPAW Platform at NC State University to validate some of the findings in this paper.

APPENDIX

A. TDOA Variance for Multi-Antenna Techniques

The total gain for the H-HV and the V-HV case are:

$$G_{\mathrm{TX}}G_{\mathrm{RX}} = |jG_y(G_z + jG_y)| = G_{\mathrm{y}}\sqrt{{G_y}^2 + {G_z}^2}\ , \quad (38)$$

$$G_{\mathrm{TX}}G_{\mathrm{RX}} = |G_z(G_z + jG_y)| = G_{\mathrm{z}}\sqrt{{G_y}^2 + {G_z}^2}\ . \quad (39)$$

Substituting ${G_y}^2 = \frac{{k_0 d_i}^2}{{\sigma^2}_{\text{i-HH}}}$ and ${G_z}^2 = \frac{{k_0 d_i}^2}{{\sigma^2}_{\text{i-VV}}}$ from (14) and (15) into (39), we get:

$${\sigma^2}_{\text{i-H-HV}} = \frac{{k_0 d_i}^2}{G_{\mathrm{y}}\sqrt{{G_y}^2 + {G_z}^2}} = \frac{\sigma^2_{\text{i-HH}}\sigma_{\text{i-VV}}}{(\sigma^2_{\text{i-HH}} + \sigma^2_{\text{i-VV}})^{\frac{1}{2}}}\ , \quad (40)$$

$${\sigma^2}_{\text{i-V-HV}} = \frac{{k_0 d_i}^2}{G_{\mathrm{z}}\sqrt{{G_y}^2 + {G_z}^2}} = \frac{\sigma^2_{\text{i-VV}}\sigma_{\text{i-HH}}}{(\sigma^2_{\text{i-HH}} + \sigma^2_{\text{i-VV}})^{\frac{1}{2}}}\ , \quad (41)$$

which are the same as the expressions stated in (16).

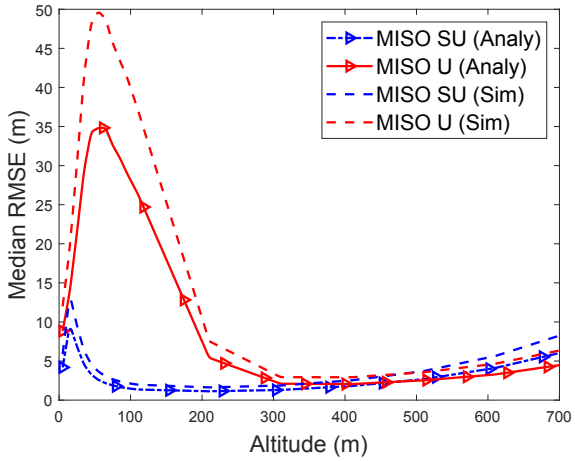

(a) 0 m $\leq h \leq$ 700 m.

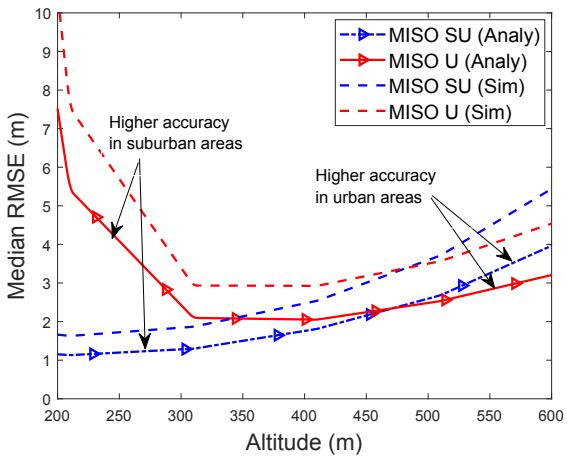

(b) 200 m $\leq h \leq$ 600 m..

Fig. 9: Median RMSE as a function of UAV altitude under mixed LoS/NLoS conditions, for MISO antenna patterns at various altitude ranges: (a) 0 m $\leq h \leq$ 700 m, and (b) 200 m $\leq h \leq$ 600 m.

B. Distribution of a Single TDOA Measurement

Case 1 ($\mathsf{S}_{\mathsf{A},i} = \mathsf{NLoS}$, $\mathsf{S}_{\mathsf{A},j} = \mathsf{NLoS}$): Using (4), the probability of having both S-i and S-j in the NLoS states are given as: $\mathbb{P}\left(\mathsf{S}_{\mathsf{A},i} = \mathsf{NLoS}, \mathsf{S}_{\mathsf{A},j} = \mathsf{NLoS}\right) = \left(1 - \mathsf{P}_{\mathsf{LoS}}(\boldsymbol{x}, \boldsymbol{x_i})\right)\left(1 - \mathsf{P}_{\mathsf{LoS}}(\boldsymbol{x}, \boldsymbol{x_j})\right)$. Since, $\hat{\tau}_i$ and $\hat{\tau}_j$ are independent, using (17) the distribution of the TDOA measurement $\hat{\tau}_{ij} = \hat{\tau}_i - \hat{\tau}_j$ is given as: $\hat{\tau}_{ij} \sim \mathcal{N}\left(\tau_i - \tau_j, \eta^{\mathsf{NLoS}}(\sigma_i^2 + \sigma_j^2) + 2\sigma_{\mathsf{b}}^2\right)$, with probability $\mathbb{P}\left(\mathsf{S}_{\mathsf{A},i} = \mathsf{NLoS}, \mathsf{S}_{\mathsf{A},j} = \mathsf{NLoS}\right)$. The distribution for the other 3 cases listed below can be obtained similarly.

Case 2 ($\mathsf{S}_{\mathsf{A},i} = \mathsf{LoS}$, $\mathsf{S}_{\mathsf{A},j} = \mathsf{NLoS}$):

$$\hat{\tau}_i \sim \mathcal{N}\left(\tau_i, \eta^{\mathsf{LoS}}\sigma_i^2\right) \ , \quad \hat{\tau}_j \sim \mathcal{N}\left(\tau_j + \mu_{\mathsf{b}}, \eta^{\mathsf{NLoS}}\sigma_j^2 + \sigma_{\mathsf{b}}^2\right) \ .$$

Case 3 ($\mathsf{S}_{\mathsf{A},i} = \mathsf{NLoS}$, $\mathsf{S}_{\mathsf{A},j} = \mathsf{LoS}$):

$$\hat{\tau}_i \sim \mathcal{N}\left(\tau_i + \mu_{\mathsf{b}}, \eta^{\mathsf{NLoS}}\sigma_i^2 + \sigma_{\mathsf{b}}^2\right) \ , \quad \hat{\tau}_j \sim \mathcal{N}\left(\tau_j, \eta^{\mathsf{LoS}}\sigma_j^2\right) \ .$$

Case 4 ($\mathsf{S}_{\mathsf{A},i} = \mathsf{LoS}$, $\mathsf{S}_{\mathsf{A},j} = \mathsf{LoS}$):

$$\hat{\tau}_i \sim \mathcal{N}\left(\tau_i, \eta^{\mathsf{LoS}}\sigma_i^2\right) \ , \quad \hat{\tau}_j \sim \mathcal{N}\left(\tau_j, \eta^{\mathsf{LoS}}\sigma_j^2\right) \ .$$

C. Conditional Distribution of TDOA Measurements

From (17) and (19), the distribution of $\hat{\tau}_i$, for a given link state, $\mathsf{S}_{\mathsf{A,i}}$, is stated as:

$$\mathbb{E}\left[\hat{\tau}_i|\mathsf{S}_{\mathsf{A,i}}\right] = \tau_i + \mu_{\mathsf{b}}\mathbb{I}_{\mathsf{N}}(\mathsf{S}_{\mathsf{A,i}}) \ , \tag{42}$$

$$\mathbb{E}\left[\hat{\tau}_i^2|\mathsf{S}_{\mathsf{A,i}}\right] - \left(\mathbb{E}\left[\hat{\tau}_i|\mathsf{S}_{\mathsf{A,i}}\right]\right)^2 = \eta^{\mathsf{LoS}}\sigma_i^2\left(1 - \mathbb{I}_{\mathsf{N}}(\mathsf{S}_{\mathsf{A,i}})\right) + (\eta^{\mathsf{NLoS}}\sigma_i^2 + \sigma_{\mathsf{b}}^2)\mathbb{I}_{\mathsf{N}}(\mathsf{S}_{\mathsf{A,i}}) \ . \tag{43}$$

Thus the mean and variance of a TDOA measurement, $\hat{\tau}_{1i}$, given the states, $\mathsf{S}_{\mathsf{A,i}}$ and $\mathsf{S}_{\mathsf{A},1}$ are:

$$\begin{aligned}\boldsymbol{\mu}(i) &= \mathbb{E}[\hat{\tau}_{1i}|\{\mathsf{S}_{\mathsf{A},1}, \mathsf{S}_{\mathsf{A,i}}\}] = \mathbb{E}[\hat{\tau}_1|\mathsf{S}_{\mathsf{A},1}] - \mathbb{E}[\hat{\tau}_i|\mathsf{S}_{\mathsf{A,i}}] \\ &= \left(\frac{d_1}{c} + \mathbb{I}_{\mathsf{N}}(\mathsf{S}_{\mathsf{A},1})\mu_{\mathsf{b}}\right) - \left(\frac{d_{i+1}}{c} + \mathbb{I}_{\mathsf{N}}(\mathsf{S}_{\mathsf{A,i}})\mu_{\mathsf{b}}\right) \\ &= \frac{(d_1 - d_{i+1})}{c} + \mu_b\Big[\mathbb{I}_{\mathsf{N}}(\mathsf{S}_{\mathsf{A},1}) - \mathbb{I}_{\mathsf{N}}(\mathsf{S}_{\mathsf{A},i+1})\Big] \ , \end{aligned} \tag{44}$$

which is the same as (22), and

$$\begin{aligned} R(i,i) &= \mathbb{E}\left[\hat{\tau}_{1i}^2\right] - \left(\mathbb{E}\left[\hat{\tau}_{1i}\right]\right)^2 \\ &= \mathbb{E}\left[\left(\hat{\tau}_1 - \hat{\tau}_i\right)^2\right] - \left(\mathbb{E}\left[\hat{\tau}_1\right] - \mathbb{E}\left[\hat{\tau}_i\right]\right)^2 \\ &= \mathbb{E}\left[\hat{\tau}_i^2|\mathsf{S}_{\mathsf{A,i}}\right] - \left(\mathbb{E}\left[\hat{\tau}_1|\mathsf{S}_{\mathsf{A},1}\right]\right)^2 - \mathbb{E}\left[\hat{\tau}_1^2|\mathsf{S}_{\mathsf{A},1}\right] - \left(\mathbb{E}\left[\hat{\tau}_i|\mathsf{S}_{\mathsf{A,i}}\right]\right)^2 \\ &= \eta^{\mathsf{LoS}}\sigma_1^2(1 - \mathbb{I}_{\mathsf{N}}(\mathsf{S}_{\mathsf{A},1})) + (\eta^{\mathsf{NLoS}}\sigma_1^2 + \sigma_{\mathsf{b}}^2)\mathbb{I}_{\mathsf{N}}(\mathsf{S}_{\mathsf{A},1}) \\ &+ \eta^{\mathsf{LoS}}\sigma_i^2(1 - \mathbb{I}_{\mathsf{N}}(\mathsf{S}_{\mathsf{A,i}}))(\eta^{\mathsf{NLoS}}\sigma_i^2 + \sigma_{\mathsf{b}}^2) \\ &= \sigma_{\mathsf{b}}^2\Big[\mathbb{I}_{\mathsf{N}}(\mathsf{S}_{\mathsf{A},1}) + \mathbb{I}_{\mathsf{N}}(\mathsf{S}_{\mathsf{A},i+1})\Big] \\ &+ \eta^{\mathsf{NLoS}}\Big[\mathbb{I}_{\mathsf{N}}(\mathsf{S}_{\mathsf{A},1})\sigma_1^2 + \mathbb{I}_{\mathsf{N}}(\mathsf{S}_{\mathsf{A},i+1})\sigma_{i+1}^2\Big] \\ &+ \ \eta^{\mathsf{LoS}}\Big[\big(1 - \mathbb{I}_{\mathsf{N}}(\mathsf{S}_{\mathsf{A},1})\big)\sigma_1^2 + \big(1 - \mathbb{I}_{\mathsf{N}}(\mathsf{S}_{\mathsf{A},i+1})\big)\sigma_{i+1}^2\Big] \ . \end{aligned} \tag{45}$$

For $i \neq j$,

$$\begin{aligned} R(i,j) &= \mathbb{E}[\hat{\tau}_{1i}\hat{\tau}_{1j}|\{\mathsf{S}_{\mathsf{A},1}, \mathsf{S}_{\mathsf{A,i}}, \mathsf{S}_{\mathsf{A,j}}\}] \\ &- \mathbb{E}[\hat{\tau}_{1i}|\{\mathsf{S}_{\mathsf{A},1}, \mathsf{S}_{\mathsf{A,i}}\}]\mathbb{E}[\hat{\tau}_{1j}|\{\mathsf{S}_{\mathsf{A},1}, \mathsf{S}_{\mathsf{A,j}}\}] \\ &= \mathbb{E}\left[\left(\hat{\tau}_1|\mathsf{S}_{\mathsf{A},1} - \hat{\tau}_i|\mathsf{S}_{\mathsf{A,i}}\right)\left(\hat{\tau}_1|\mathsf{S}_{\mathsf{A},1} - \hat{\tau}_j|\mathsf{S}_{\mathsf{A,j}}\right)\right] \\ &- \left(\mathbb{E}\left[\hat{\tau}_1|\mathsf{S}_{\mathsf{A},1}\right] - \mathbb{E}\left[\hat{\tau}_i|\mathsf{S}_{\mathsf{A,i}}\right]\right)\left(\mathbb{E}\left[\hat{\tau}_1|\mathsf{S}_{\mathsf{A},1}\right] - \mathbb{E}\left[\hat{\tau}_j|\mathsf{S}_{\mathsf{A,j}}\right]\right) \\ &= \mathbb{E}\left[\hat{\tau}_1^2|\mathsf{S}_{\mathsf{A},1}\right] - \left(\mathbb{E}\left[\hat{\tau}_1|\mathsf{S}_{\mathsf{A},1}\right]\right)^2 \\ &= \sigma_{\mathsf{b}}^2\mathbb{I}_{\mathsf{N}}(\mathsf{S}_{\mathsf{A},1}) + \eta^{\mathsf{NLoS}}\Big[\mathbb{I}_{\mathsf{N}}(\mathsf{S}_{\mathsf{A},1})\sigma_1^2\Big] \\ &+ \eta^{\mathsf{LoS}}\Big[\big(1 - \mathbb{I}_{\mathsf{N}}(\mathsf{S}_{\mathsf{A},1})\big)\sigma_1^2\Big] \ , \end{aligned} \tag{46}$$

which are same as the expressions given in (23).

D. FIM in Mixed LoS/NLoS Environment

We define the following:

$$g\left(\boldsymbol{x}, \boldsymbol{s}\right) = \frac{1}{2}\left(\boldsymbol{z} - \boldsymbol{\mu}\left(\boldsymbol{x}, \boldsymbol{s}\right)\right)^T \boldsymbol{R}^{-1}\left(\boldsymbol{x}, \boldsymbol{s}\right)\left(\boldsymbol{z} - \boldsymbol{\mu}\left(\boldsymbol{x}, \boldsymbol{s}\right)\right) \ ,$$

to rewrite (24) as $p\left(\boldsymbol{z}|\boldsymbol{x},\boldsymbol{s}\right)=\frac{\exp\left(-g(\boldsymbol{x},\boldsymbol{s})\right)}{\sqrt{2\pi|\boldsymbol{R}(\boldsymbol{x},\boldsymbol{s})|}}$. Thus we get:

$$\begin{aligned}
&\frac{\partial p(\boldsymbol{z}|\boldsymbol{x},\boldsymbol{s})}{\partial x_i}=-\frac{\left(|\boldsymbol{R}\left(\boldsymbol{x},\boldsymbol{s}\right)|^{-1}\exp\left(-g\left(\boldsymbol{x},\boldsymbol{s}\right)\right)\frac{\partial g(\boldsymbol{x},\boldsymbol{s})}{\partial x_i}\right)}{\sqrt{2\pi}}\\
&+\frac{\left(-\frac{1}{2}|\boldsymbol{R}\left(\boldsymbol{x},\boldsymbol{s}\right)|^{\frac{-3}{2}}\exp\left(-g\left(\boldsymbol{x},\boldsymbol{s}\right)\right)\frac{\partial|\boldsymbol{R}(\boldsymbol{x},\boldsymbol{s})|}{\partial x_i}\right)}{\sqrt{2\pi}}\\
&=-\frac{\left(\frac{1}{2}|\boldsymbol{R}\left(\boldsymbol{x},\boldsymbol{s}\right)|^{\frac{-1}{2}}\frac{\partial|\boldsymbol{R}(\boldsymbol{x},\boldsymbol{s})|}{\partial x_i}+\frac{\partial g(\boldsymbol{x},\boldsymbol{s})}{\partial x_i}\right)e^{-g(\boldsymbol{x},\boldsymbol{s})}}{\sqrt{2\pi|\boldsymbol{R}\left(\boldsymbol{x},\boldsymbol{s}\right)|}}\\
&=-p\left(\boldsymbol{z}|\boldsymbol{x},\boldsymbol{s}\right)\left(\frac{1}{2}|\boldsymbol{R}\left(\boldsymbol{x},\boldsymbol{s}\right)|^{-\frac{1}{2}}\frac{\partial|\boldsymbol{R}(\boldsymbol{x},\boldsymbol{s})|}{\partial x_i}+\frac{\partial g\left(\boldsymbol{x},\boldsymbol{s}\right)}{\partial x_i}\right)\\
&=\frac{-p\left(\boldsymbol{z}|\boldsymbol{x},\boldsymbol{s}\right)}{2}|\boldsymbol{R}\left(\boldsymbol{x},\boldsymbol{s}\right)|^{\frac{1}{2}}\mathrm{Tr}\left(\boldsymbol{R}^{-1}\left(\boldsymbol{x},\boldsymbol{s}\right)\frac{\partial\boldsymbol{R}^{T}(\boldsymbol{x},\boldsymbol{s})}{\partial x_i}\right)\\
&-\frac{p\left(\boldsymbol{z}|\boldsymbol{x},\boldsymbol{s}\right)}{2}\frac{\partial\Big(\left(\boldsymbol{z}-\boldsymbol{\mu}\left(\boldsymbol{x},\boldsymbol{s}\right)\right)^{T}\boldsymbol{R}^{-1}\left(\boldsymbol{x},\boldsymbol{s}\right)\left(\boldsymbol{z}-\boldsymbol{\mu}\left(\boldsymbol{x},\boldsymbol{s}\right)\right)\Big)}{\partial x_i}\\
&=\frac{-p\left(\boldsymbol{z}|\boldsymbol{x},\boldsymbol{s}\right)}{2}|\boldsymbol{R}\left(\boldsymbol{x},\boldsymbol{s}\right)|^{\frac{1}{2}}\mathrm{Tr}\left(\boldsymbol{R}^{-1}\left(\boldsymbol{x},\boldsymbol{s}\right)\frac{\partial\boldsymbol{R}^{T}(\boldsymbol{x},\boldsymbol{s})}{\partial x_i}\right)\\
&+p\left(\boldsymbol{z}|\boldsymbol{x},\boldsymbol{s}\right)\left[\frac{\partial\boldsymbol{\mu}^{T}(\boldsymbol{x},\boldsymbol{s})}{\partial x_i}\boldsymbol{R}^{-1}(\boldsymbol{x},\boldsymbol{s})\big(\boldsymbol{z}-\mu(\boldsymbol{x},\boldsymbol{s})\big)\right]\\
&-\left[\frac{p\left(\boldsymbol{z}|\boldsymbol{x},\boldsymbol{s}\right)}{2}\big(\boldsymbol{z}-\mu(\boldsymbol{x},\boldsymbol{s})\big)^{T}\frac{\partial\boldsymbol{R}^{-1}(\boldsymbol{x},\boldsymbol{s})}{\partial x_i}\big(\boldsymbol{z}-\mu(\boldsymbol{x},\boldsymbol{s})\big)\right].
\end{aligned}\tag{47}$$

Next we compute $\frac{\partial\mathbb{P}(\boldsymbol{S}=\boldsymbol{s})}{\partial x_i}$ as an explicit function of the marginal pdf $p(z|x,s)$, in (48). Substituting (47) and (48), into $\frac{\partial p(\boldsymbol{z}|\boldsymbol{x})}{\partial x_i}=\sum_s p\left(\boldsymbol{z}|\boldsymbol{x},\boldsymbol{s}\right)\frac{\partial\mathbb{P}(\boldsymbol{S}=\boldsymbol{s})}{\partial x_i}+\sum_s\mathbb{P}(\boldsymbol{S}=\boldsymbol{s})\frac{\partial p(\boldsymbol{z}|\boldsymbol{x},\boldsymbol{s})}{\partial x_i}$, we obtain (29). Finally, defining $f(\boldsymbol{x})=\frac{-180b}{\pi}\tan^{-1}\left(\frac{h}{r_m(\boldsymbol{x})}\right)$, we rewrite (4) as $\mathsf{P}_{\mathsf{LoS}}(\boldsymbol{x},\boldsymbol{x_m})=\frac{1}{1+a\exp\left(f(\boldsymbol{x})\right)}$ and obtain:

$$\begin{aligned}
&\frac{\partial\mathsf{P}_{\mathsf{LoS}}(\boldsymbol{x},\boldsymbol{x_m})}{\partial x_k}=\frac{-ae^{f(\boldsymbol{x})}}{\left(1+ae^{f(\boldsymbol{x})}\right)^2}\frac{\partial f\left(\boldsymbol{x}\right)}{\partial x}=\frac{180ab}{\pi\left(1+ae^{f(\boldsymbol{x})}\right)}\\
&\times\left(1-\frac{1}{1+ae^{(f(\boldsymbol{x}))}}\right)\frac{{r_m}^2}{{r_m}^2+h^2}\frac{\partial}{\partial x_k}\left(\frac{h}{r_m(\boldsymbol{x})}\right).
\end{aligned}\tag{49}$$

E. Single Antenna FIM

Using (1), (2), and (14) we get: $\sigma^2_{\text{i-VV}}={r_i}^2\cos^{-2}\left(\beta\right)$, and $\sigma^2_{\text{i-HH}}=\psi_i(x,h)\cos^{-2}\left(\theta\right)$. Differentiating these with respect to x, we get the terms $\frac{\partial\sigma^2_{\text{i-HH}}}{\partial x}$ and $\frac{\partial\sigma^2_{\text{i-VV}}}{\partial x}$ in (32).

F. Multi Antenna FIM

Differentiating the first equation in (16), we get:

$$\begin{aligned}
&\frac{\partial\sigma^2_{\text{i-V-HV}}}{\partial x_i}=\frac{\partial\sigma^2_{\text{i-V-HV}}}{\partial\sigma^2_{\text{i-HH}}}\frac{\partial\sigma^2_{\text{i-HH}}}{\partial x_i}+\frac{\partial\sigma^2_{\text{i-V-HV}}}{\partial\sigma^2_{\text{i-VV}}}\frac{\partial\sigma^2_{\text{i-VV}}}{\partial x_i}\\
&=\frac{1}{2\sigma_{\text{i-HH}}\left(\sigma^{-2}_{\text{i-HH}}+\sigma^{-2}_{\text{i-VV}}\right)^{\frac{1}{2}}}\frac{\partial\sigma^2_{\text{i-HH}}}{\partial x_i}+\frac{\sigma_{\text{i-HH}}}{2\sigma_{\text{i-HH}}\left(\sigma^{-2}_{\text{i-HH}}+\sigma^{-2}_{\text{i-VV}}\right)^{\frac{3}{2}}}\\
&\times\left(\sigma^{-4}_{\text{i-HH}}\frac{\partial\sigma^2_{\text{i-HH}}}{\partial x_i}+\sigma^{-4}_{\text{i-VV}}\frac{\partial\sigma^2_{\text{i-VV}}}{\partial x_i}\right).
\end{aligned}\tag{50}$$

Simple algebraic manipulation yields the first equation in (37), and the second can be obtained similarly.

REFERENCES

[1] Y. Zeng, R. Zhang, and T. J. Lim, "Wireless communications with unmanned aerial vehicles: opportunities and challenges," *IEEE Commun. Mag.*, vol. 54, no. 5, pp. 36–42, May 2016.

[2] I. Guvenc, F. Koohifar, S. Singh, M. L. Sichitiu, and D. Matolak, "Detection, tracking, and interdiction for amateur drones," *IEEE Commun. Mag.*, vol. 56, no. 4, pp. 75–81, 2018.

[3] M. M. Azari, H. Sallouha, A. Chiumento, S. Rajendran, E. Vinogradov, and S. Pollin, "Key technologies and system trade-offs for detection and localization of amateur drones," *IEEE Commun. Mag.*, vol. 56, no. 1, pp. 51–57, 2018.

[4] K. Chang, "RF sensor for interference detection-an RF signal-based drone detection system," *KeySight Technologies*, 2016.

[5] T. Boon-Poh, "RF techniques for detection, classification and location of commercial drone controllers," *KeySight Technologies, Aerospace Defense Symposium*, 2017.

[6] S. Gezici, "A survey on wireless position estimation," *Wireless Pers. Commun.*, vol. 44, no. 3, pp. 263–282, Feb. 2008.

[7] J. Chen, D. Raye, W. Khawaja, P. Sinha, and I. Guvenc, "Impact of 3D UWB Antenna Radiation Pattern on Air-to-Ground Drone Connectivity," in *Proc. IEEE Vehic. Technol. Conf. (VTC)*, Chicago, IL, Sep. 2018.

[8] I. Guvenc and C. Chong, "A survey on TOA based wireless localization and NLOS mitigation techniques," *IEEE Commun. Surveys Tutorials*, vol. 11, no. 3, pp. 107–124, 2009.

[9] X. Shi, G. Mao, Z. Yang, and J. Chen, "MLE-based localization and performance analysis in probabilistic LOS/NLOS environment," *Neurocomputing*, vol. 270, pp. 101 – 109, 2017.

[10] P. Sinha, Y. Yapici, and I. Guvenc, "Impact of 3D antenna radiation patterns on TDOA-based wireless localization of UAVs," in *Proc. IEEE INFOCOM Workshops*, Paris, France, Apr. 2019, pp. 614–619.

[11] E. Yanmaz, R. Kuschnig, and C. Bettstetter, "Achieving air-ground communications in 802.11 networks with three-dimensional aerial mobility," in *Proc. IEEE INFOCOM*, Turin, Italy, Apr. 2013, pp. 120–124.

[12] ——, "Channel measurements over 802.11a-based UAV-to-ground links," in *Proc. IEEE GLOBECOM Wkshps.*, Houston, TX, Dec. 2011, pp. 1280–1284.

[13] X. Yang, Y. Qi, B. Yuan, Y. Cao, and G. Wang, "A miniaturized high-gain flexible antenna for UAV applications," *Int. J. of Ant. Prop.*, vol. 2021, p. 9919425.

[14] M. Badi, J. Wensowitch, D. Rajan, and J. Camp, "Experimentally analyzing diverse antenna placements and orientations for UAV communications," *IEEE Trans. Veh. Technol.*, vol. 69, no. 12, pp. 14 989–15 004, 2020.

[15] U. Bhattacherjee, E. Ozturk, O. Ozdemir, I. Guvenc, M. L. Sichitiu, and H. Dai, "Experimental study of outdoor UAV localization and tracking using passive RF sensing," *in Proc. IEEE/ACM WiNTECH Workshop*, Nov. 2021.

[16] S. Tomic, M. Beko, and R. Dinis, "3-D target localization in wireless sensor networks using RSS and AoA measurements," *IEEE Trans. Veh. Technol.*, vol. 66, no. 4, pp. 3197–3210, 2017.

[17] Y. Chan, F. Chan, W. Read, B. Jackson, and B. Lee, "Hybrid localization of an emitter by combining angle-of-arrival and received signal strength measurements," in *Proc. IEEE Canadian Conf. Electric Comp. Eng.*, 2014, pp. 1–5.

[18] L. Zhang, T. Du, and C. Jiang, "RSSD-based 3-D localization of an unknown radio transmitter using weighted least square and factor graph," *EURASIP J. Wireless Commun. Netw.*, vol. 2019, no. 1, p. 10, 2019.

[19] Q. Qi, Y. Li, Y. Wu, Y. Wang, Y. Yue, and X. Wang, "RSS-AOA-based localization via mixed semi-definite and second-order cone relaxation in 3-D wireless sensor networks," *IEEE Access*, vol. 7, pp. 117 768–117 779, 2019.

[20] S. Chang, Y. Zheng, P. An, J. Bao, and J. Li, "3-D RSS-AOA based target localization method in wireless sensor networks using convex relaxation," *IEEE Access*, vol. 8, pp. 106 901–106 909, 2020.

[21] Q. Wang, Z. Duan, and X. R. Li, "Three-dimensional location estimation using biased RSS measurements," *IEEE Trans. Aerosp. Electron. Syst.*, vol. 56, no. 6, pp. 4673–4688, 2020.

[22] K. Yu, "3-D localization error analysis in wireless networks," *IEEE Trans. Wireless Commun.*, vol. 6, no. 10, pp. 3472–3481, 2007.

[23] D. T. A. Nguyen, J. Joung, and X. Kang, "Deep gated recurrent unit-based 3D localization for UWB systems," *IEEE Access*, vol. 9, pp. 68 798–68 813, 2021.

[24] Y. Li, F. Shu, B. Shi, X. Cheng, Y. Song, and J. Wang, "Enhanced RSS-based UAV localization via trajectory and multi-base stations," *IEEE Commun. Lett.*, vol. 25, no. 6, pp. 1881–1885, 2021.

$$\frac{\partial \mathbb{P}(\boldsymbol{S}=\boldsymbol{s})}{\partial x_i} = \prod_{\boldsymbol{s}(n)=\mathsf{NLoS}} \left(1-\mathsf{P}_{\mathsf{LoS}}\left(\boldsymbol{x},\boldsymbol{x_n}\right)\right) \sum_{\boldsymbol{s}(m)=\mathsf{LoS}} \left(\frac{\partial \mathsf{P}_{\mathsf{LoS}}(\boldsymbol{x},\boldsymbol{x_m})}{\partial x_i} \frac{\prod_{\boldsymbol{s}(k)=\mathsf{LoS}} \mathsf{P}_{\mathsf{LoS}}(\boldsymbol{x},\boldsymbol{x_k})}{\mathsf{P}_{\mathsf{LoS}}(\boldsymbol{x},\boldsymbol{x_m})} \right) - \prod_{\boldsymbol{s}(m)=\mathsf{LoS}} \mathsf{P}_{\mathsf{LoS}}\left(\boldsymbol{x},\boldsymbol{x_m}\right) \times$$

$$\sum_{\boldsymbol{s}(n)=\mathsf{NLoS}} \left(\frac{\partial \mathsf{P}_{\mathsf{LoS}}(\boldsymbol{x},\boldsymbol{x_n})}{\partial x_i} \frac{\prod_{\boldsymbol{s}(k)=\mathsf{NLoS}} \left(1-\mathsf{P}_{\mathsf{LoS}}(\boldsymbol{x},\boldsymbol{x_k})\right)}{1-\mathsf{P}_{\mathsf{LoS}}\left(\boldsymbol{x},\boldsymbol{x_n}\right)} \right) = \prod_{\boldsymbol{s}(n)=\mathsf{NLoS}} \left(1-\mathsf{P}_{\mathsf{LoS}}\left(\boldsymbol{x},\boldsymbol{x_n}\right)\right) \prod_{\boldsymbol{s}(k)=\mathsf{LoS}} \mathsf{P}_{\mathsf{LoS}}(\boldsymbol{x},\boldsymbol{x_k}) \times$$

$$\sum_{\boldsymbol{s}(m)=\mathsf{LoS}} \left(\frac{\partial \mathsf{P}_{\mathsf{LoS}}(\boldsymbol{x},\boldsymbol{x_m})}{\partial x_i} \frac{1}{\mathsf{P}_{\mathsf{LoS}}(\boldsymbol{x},\boldsymbol{x_m})} \right) - \prod_{\boldsymbol{s}(m)=\mathsf{LoS}} \mathsf{P}_{\mathsf{LoS}}\left(\boldsymbol{x},\boldsymbol{x_m}\right) \prod_{\boldsymbol{s}(k)=\mathsf{NLoS}} \left(1-\mathsf{P}_{\mathsf{LoS}}(\boldsymbol{x},\boldsymbol{x_k})\right) \sum_{\boldsymbol{s}(n)=\mathsf{NLoS}} \left(\frac{\partial \mathsf{P}_{\mathsf{LoS}}(\boldsymbol{x},\boldsymbol{x_n})}{\partial x_i} \frac{1}{1-\mathsf{P}_{\mathsf{LoS}}\left(\boldsymbol{x},\boldsymbol{x_n}\right)} \right)$$

$$= \sum_{m:\boldsymbol{s}(m)=\mathsf{LoS}} \frac{\mathbb{P}(\boldsymbol{S}=\boldsymbol{s})}{\mathsf{P}_{\mathsf{LoS}}(\boldsymbol{x},\boldsymbol{x_m})} \frac{\partial \mathsf{P}_{\mathsf{LoS}}(\boldsymbol{x},\boldsymbol{x_m})}{\partial x_i} - \sum_{n:\boldsymbol{s}(n)=\mathsf{NLoS}} \frac{\mathbb{P}(\boldsymbol{S}=\boldsymbol{s})}{1-\mathsf{P}_{\mathsf{LoS}}(\boldsymbol{x},\boldsymbol{x_n})} \frac{\partial \mathsf{P}_{\mathsf{LoS}}(\boldsymbol{x},\boldsymbol{x_n})}{\partial x_i} . \tag{48}$$

[25] I. A. Meer, M. Ozger, and C. Cavdar, "On the localization of unmanned aerial vehicles with cellular networks," in *Proc. IEEE Wireless Commun. Netw. Conf. (WCNC)*, 2020, pp. 1–6.

[26] X. Wei, N. Palleit, and T. Weber, "AOD/AOA/TOA-based 3D positioning in NLOS multipath environments," in *Proc. IEEE Int. Symp. Personal, Indoor, and Mobile Radio Commun. (PIMRC)*, Toronto, Canada, Sep. 2011, pp. 1289–1293.

[27] C. Xu, J. He, X. Zhang, S. Duan, and C. Yao, "3D localization performance evaluation using IMU/TOA fusion methods," *Int. J. Wireless Inform. Netw.*, vol. 26, no. 2, pp. 67–79, Jun 2019.

[28] C. Wu, X. Yi, W. Wang, L. You, Q. Huang, and X. Gao, "Learning to localize: A 3D CNN approach to user positioning in massive MIMO-OFDM systems," 2019.

[29] A. Şahin, Y. S. Eroğlu, Güvenç, N. Pala, and M. Yüksel, "Hybrid 3-D localization for visible light communication systems," *IEEE J. Lightwave Technol.*, vol. 33, no. 22, pp. 4589–4599, 2015.

[30] S. Wang and X. Jiang, "Three-dimensional cooperative positioning in vehicular ad-hoc networks," *IEEE Trans. Intelligent Transp. Syst.*, vol. 22, no. 2, pp. 937–950, 2021.

[31] X. Jiang and S. Wang, "Three-dimensional cooperative positioning for VANETs with AOA measurements," in *Proc. IEEE Wireless Commun. Netw. Conf.*, Nanjing, China, Apr. 2021, pp. 1–6.

[32] M. M. Azari, F. Rosas, and S. Pollin, "Cellular connectivity for UAVs: Network modeling, performance analysis, and design guidelines," *IEEE Trans. Wireless Commun.*, vol. 18, no. 7, p. 3366–3381, Jul 2019.

[33] M. M. Azari, Y. Murillo, O. Amin, F. Rosas, M. Alouini, and S. Pollin, "Coverage maximization for a poisson field of drone cells," in *Proc. IEEE Int. Symp. Personal, Indoor, and Mobile Radio Commun. (PIMRC)*, 2017, pp. 1–6.

[34] M. Ezuma, F. Erden, C. Kumar Anjinappa, O. Ozdemir, and I. Guvenc, "Detection and classification of UAVs using RF fingerprints in the presence of Wi-Fi and Bluetooth interference," *IEEE Open J. Commun. Soc.*, vol. 1, pp. 60–76, 2020.

[35] J. Barry, J. Kahn, W. Krause, E. Lee, and D. Messerschmitt, "Simulation of multipath impulse response for indoor wireless optical channels," *IEEE J. Select. Areas. Commun.*, vol. 11, no. 3, pp. 367–379, 1993.

[36] A. Al-Hourani, S. Kandeepan, and S. Lardner, "Optimal LAP altitude for maximum coverage," *IEEE Wireless Commun. Lett.*, vol. 3, no. 6, pp. 569–572, Dec. 2014.

[37] F. T. Ulaby, E. Michielssen, and U. Ravaioli, "Fundamentals of applied electromagnetics," *Boston, Massachussetts: Prentice Hall*, 2010.

[38] J. Chen, D. Raye, W. Khawaja, P. Sinha, and I. Guvenc, "Impact of 3D UWB antenna radiation pattern on Air-to-Ground drone connectivity," in *Proc. IEEE Veh. Technol. Conf. (VTC)*, Chicago, IL, Aug. 2018, pp. 1–5.

[39] M. M. Uddin Chowdhury, S. Joon Maeng, I. Guvenc, and E. Bulut, "Effects of 3D antenna radiation and two-hop relaying on optimal UAV trajectory in cellular networks," in *Proc. IEEE Aerospace Conf.*, Big Sky, MT, Mar. 2019, pp. 1–11.

[40] S. M. Kay, *Fundamentals of Statistical Signal Processing: Estimation Theory*. Upper Saddle River, NJ, USA: Prentice-Hall, Inc., 1993.

[41] R. Zekavat and R. M. Buehrer, *Handbook of Position Location: Theory, Practice and Advances*, 1st ed. Wiley-IEEE Press, 2011.

[42] S. J. Maeng, M. A. Deshmukh, I. Guvenc, and A. Bhuyan, "Interference mitigation scheme in 3D topology IoT network with antenna radiation pattern," in *Proc. IEEE Veh. Technol. Conf. (VTC)*, Honolulu, HI, Sep. 2019, pp. 1–6.

[43] Z. Sahinoglu, S. Gezici, and I. Güvenc, *Ultra-wideband Positioning Systems: Theoretical Limits, Ranging Algorithms, and Protocols*. Cambridge University Press, 2008.

[44] A. Carlson, P. Crilly, and J. Rutledge, *Communication Systems: An Introduction to Signals and Noise in Electrical Communication*. McGraw-Hill, 2002.

[45] R. Fletcher, *Introduction To Practical Methods of Optimization*. John Wiley & Sons, Ltd, 2013, ch. 7, pp. 137–149.